Multiphase Microfluidics for Convective Heat Transfer and Manufacturing

Amy Rachel Betz

Submitted in partial fulfillment of the
requirements for the degree of
Doctor of Philosophy
in the Graduate School of Arts and Sciences

COLUMBIA UNIVERSITY

2011

Abstract

Multiphase Microfluidics for Convective Heat Transfer and Manufacturing

by

Amy Rachel Betz

Due to the length scales in microfluidic systems interfacial forces dominate over inertia and gravity. In this work, I have designed, fabricated and studied several systems that manipulate interfacial forces for manufacturing and enhance convective heat transfer. These systems have application in drug delivery, biological and chemical micro-reactors, and electronics cooling. First, fluid-fluid interfaces can be used for the generation of particles. At the interface between two fluids in motion, instabilities can occur. One reason for these instabilities is the difference in shear velocities which causes waves to propagate at the interface. With the correct geometric configuration this phenomena will lead to droplet break up. Second, liquid-gas interfaces can enhance heat and mass transfer. If air bubbles, larger than the channel diameter, are confined to a liquid filled microfluidic channel they will elongate into plugs. These plugs are surrounded by a thin liquid film, which causes the bubbles to faster than the liquid creating a recirculating wake behind the bubble. This can be used to enhance mixing in the channel but it can also increase the heat and mass transfer between the liquid and channel wall. Third, solid-liquid interfaces can enhance and control boiling. In nucleate pool boiling, single bubbles form and depart from the wall. The frequency and size of the bubbles at departure can be influenced by the surface wettability. By patterning surfaces with wetting and non-wetting regions the growth of bubbles can be controlled to enhance the heat transfer.

Table of Contents

Nomenclature

A = area (m^2)
B = hydraulic coefficient (dimensionless)
Bo = Bond number ($\rho g d^2/\sigma$)
Ca = capillary number ($\mu U/\sigma$)
c = specific heat (J/kgK)
C = gas constant
CHF = critical heat flux (W/cm^2)
d = hydraulic diameter (m)
D = diffusivity (m^2/s^2)
f = volumetric flow rate (m^3/s)
$\tilde{f}$ = frequency (Hz)
fr = friction factor (dimensionless)
G = mass velocity (kg/m^2s)
h, HTC = heat transfer coefficient (W/m^2K)
H = height (m)
k = thermal conductivity (W/mK)
K = minor loss term (dimensionless)
L = length (m)
M = mass transfer coefficient (m/s)
n = number of bubbles
n_a' = number of active nucleation site ($sites/m^2$)
N= number of channels
p = pressure (Pa)
P = perimeter (m)
Pr = Prandtl Number (ν/α)
Nu = Nusselt Number (hd/k)
$\dot{Q}$ = heat flow (W)
q"= heat flux (W/m^2)
r = radius (m)
R = radius of curvature (m)
Re = Reynolds Number ($\rho Ud/\mu$)
Sh = Sherwood number (Md/D)
t = time (s)
T = temperature (˚C)
U = velocity (m/s)
V = volume (m^3)
w = width (m)
We = Weber number ($\rho U^2 d/\sigma$)

Greek Letters
α = fin enhancement factor (dimensionless)
α^* = aspect ratio (dimensionless)
β= temperature difference ($^\circ$C)
δ= film thickness (m)
ε= liquid fraction (dimensionless)
η= fin efficiency (dimensionless)
θ = thermal resistance (K/W)
μ= viscosity (Pa·s)
ρ= density (kg/m^3)
σ = surface tension (N/m)

Subscripts
B = bubble
c = channel
con = contact
d = departure
G= gas
L = liquid
meas = measure
S = surface
sat = saturation
seg = segmented flow
sin = single phase flow
slug = liquid slug
sub = substrate
w= wall

List of figures

Dedication

This thesis is dedicated to my husband, Paul Busetti, and everyone else who helped me along my journey.

Acknowledgements

I would like to acknowledge the help, input and intellectual support from my advisor, Daniel Attinger. I would also like to thank and acknowledge my thesis committee: Yoav Peles, James Hone, Chee Wei Wong and Arvind Narayanaswamy for their insight and contributions. I would like to thank my lab mates: Mike, Jie, Raj, Junfeng and Erik for being there when research was hard and making sure I never gave up. I would also like to acknowledge my husband. It is not easy to live with a PhD student for 5 years, thanks for seeing me through.

1 INTRODUCTION

1.1 A primer on microfluidics

Microfluidics is a relatively new field emerging in the late 1980's [1]. It is a multidisciplinary filed that explores the scientific phenomena and application involving fluid dynamics on scales small enough to effect the balance of forces in the system, ranging from a few millimeters to a few microns. In microfluidics systems, surface forces are typically stronger than bulk forces due to the high surface-to-volume ratio. Let's look for instance at a sessile drop on a surface. If you were to invert the surface, as shown in Figure 1, so the drop is suspended in air, the fate of the drop (does it stick or fall?) is determined by the balance of gravity to the surface tension force $\rho Vg = 2\pi\sigma R\sin^2\theta$. The shape of the drop is controlled by the wetting angle, θ. If we assume a wetting angle of 90º, the drop will be hemispherical and we can write the force balance as $\rho\frac{2}{3}\pi R^3 g = 2\pi\sigma R$ or $R = \sqrt{\frac{\sigma}{\rho g}}$. For a water droplet the critical radius is 2.7 mm, therefore drops with a radius smaller than 2.7 mm will adhere to the surface, seemingly contradicting Newton's falling apple experience, due to the strong surface tension force. To demonstrate the dynamic behavior of the drop, we bring another surface in contact with the drop, as shown in Figure 1b. The change in the free surface will cause oscillation due to the transfer of surface energy to inertia.

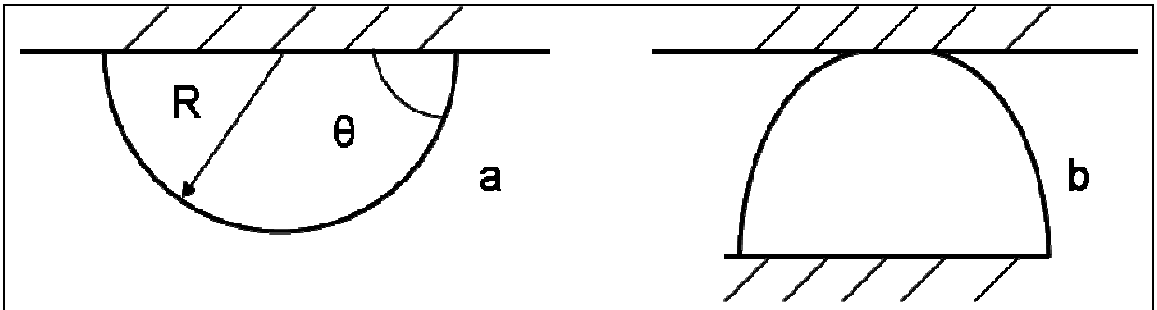

Figure 1. Depiction of a sessile drop, where R < 2.7 mm and θ = 90° , suspended from a surface (a) and the change in free surface shape when another surface is brought into contact with the drop (b).

Microfluidics is a technological application driven field [2]. Most applications for microfluidics are in chemical and biological sciences. Microfluidics devices are commonly referred to as Lab-on-a-chip applications because they seek to shrink lab processes such as PCR and flow cytometry into a microfluidic chip. This enables researchers to use smaller reagent sizes, less energy and decrease process times [3].

Microfluidics has also been explored for heat transfer applications [4]. Even though the flow in microchannels is usually laminar, the enhanced surface-to-volume ratio can increase the effective heat transfer.

1.2 Definitions

In the literature the use of the term multiphase flow varies. For the purpose of clarity in this thesis the following definitions will be used:

- Multiphase flow consists of a single fluid in multiple phases, for example water and steam flowing in a heat transfer pipe.

- Two-phase flow consists of two immiscible fluids such as water and air or water and oil. Depending on the interfacial tension of the two fluids one fluid with be the dispersed phase (drops or bubbles suspended in the flow) and the continuous phase.
- Segmented flow, shown in Figure 2, is a subset of two-phase flow, where the flow is confined to a small channel. When two immiscible fluids are confined to a small enough channel surface tension dominates over gravity and the orientation of the systems does not affect the bubble shape. In this regime one fluid will wet the surfaces of the channel and the other will be dispersed along the channel.

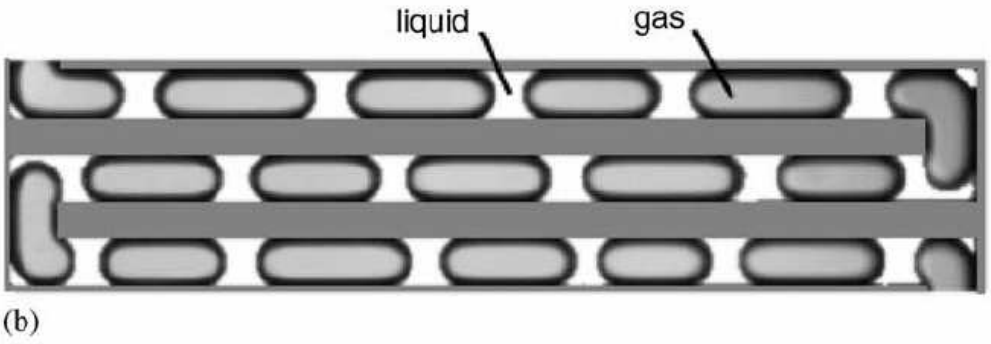

Figure 2. An example of segmented flow from [5]

It should also be noted that for brevity, if a topic includes both multiphase and two-phase flow, multiphase will be used in the title.

1.3 Multiphase flow to enhance/control transport phenomena

Multiphase microfluidics can enhance both mass and heat transfer. In two-phase flow drops, bubbles and particles have been show to enhance mass transfer [3]. Segmented flow increases both mixing and fluid to wall mass transfer [6]. The addition of interfaces

changes the behavior of the bulk fluid flow causing recirculating wakes to form behind the dispersed phase [6] as shown in Figure 3.

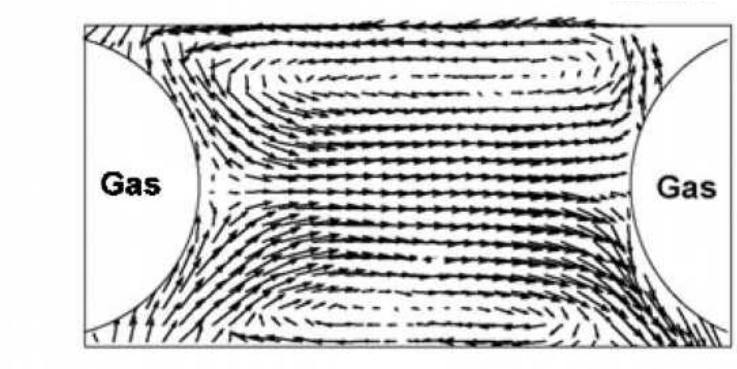

Figure 3. The recirculating wakes formed by segmented flow, measured using μ-PIV [7]

The addition of particles has also been shown to enhance mixing [8]. This is due to the inertial effects on the particle. If the particle spans a significant portion of the channel it experiences different velocity on each side causing the particle to rotate, which generates vortices in the bulk fluid. Heat transfer is enhanced in multiphase systems because there is an opportunity to take advantage of the latent heat of vaporization of a fluid. The ideal regime for multiphase heat transfer is nucleate boiling. In this regime bubbles grow and detach from the liquid/solid interface. After they detach the surface is rewetted with liquid and the process continues. In a pool boiling system the bubbles detached from the surface due to buoyancy and in flow boiling bubbles are removed by the shear force of the flow. This regime is ideal because heat is transfer directly into the liquid and vapor does not form an insulating barrier.

1.4 Tools to engineer multiphase flow in microfluidics

1.4.1 Drop and bubble generation

There are many ways to generate drops and bubbles in microfluidics. Two methods for continuous drop generation presented in this work are cross-flowing streams (also referred to as a t-junction) and flow focusing (also referred to as a co-flowing streams).

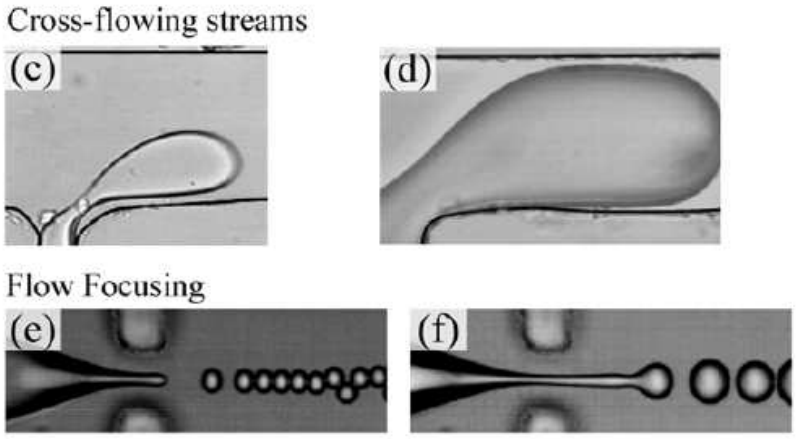

Figure 4: Continuous methods for droplet generation as presented in [9]

The breakup of drops and bubbles in microfluidics devices can be driven by pressure, shear force or instabilities.

1.4.2 Surface engineering

In microfluidic systems surface modification plays an important role due to the dominance of surface forces, as mentioned in section 1.1. Surfaces can be modified by changing their chemical and physical properties. Chemical alterations to a surface can change the surface energy, surface charge and slip and wetting properties. Physical alterations can also change wetting properties, surface roughness, friction factors and available surface area. There has been a great deal of interest for surface engineering in

microfluidic systems to control the transport properties [10]. Current manufacturing techniques use both physical and chemical approaches to create superhydrophilic and superhydrophobic surfaces [11].

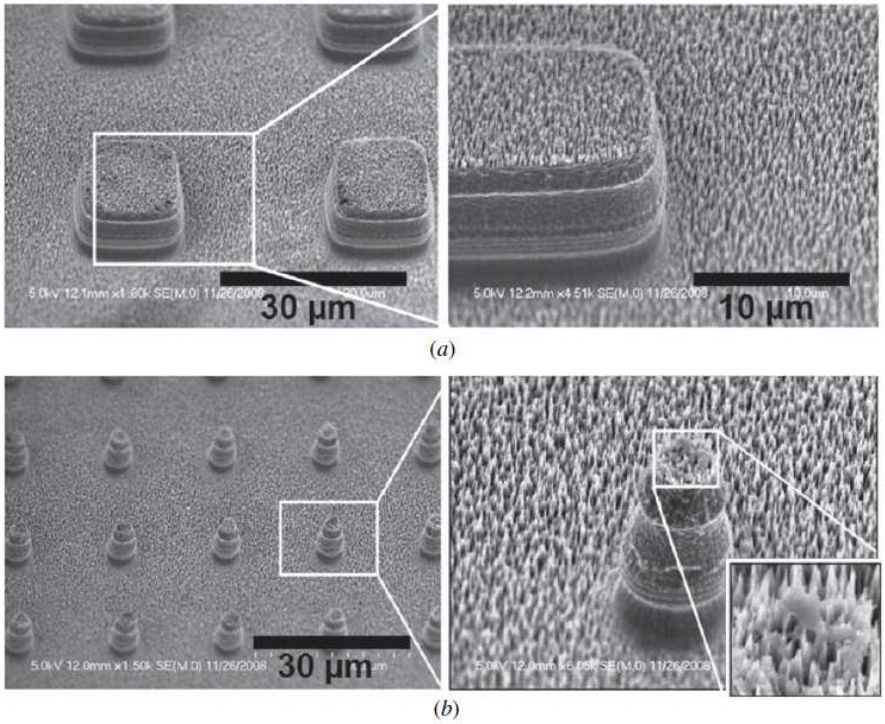

Figure 5. Deep reactive ion etching can be used to create dual micro/nano structures that mimic the lotus leaf effect [12].

There is also interest in designing dual structured micro and nanoscale surfaces [12-15], shown in Figure 5, these multiscale surfaces mimic many of the surfaces found in nature, as shown in Figure 6, and their surface performance spans multiple length scales.

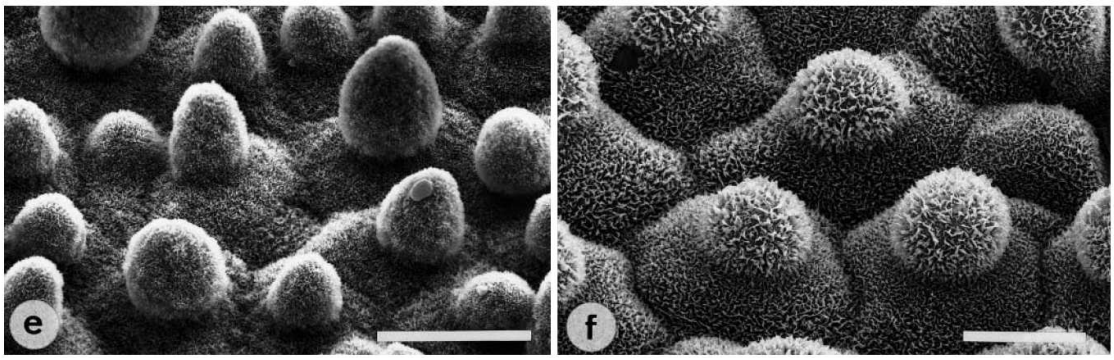

Figure 6. Scanning electron microscope (SEM) images of a naturally superhydrophobic surfaces of the lotus leaf (left) and a Taro plant (right)[14]. The scale bar on the image is 20 µm.

Using the combination of micro and nanofabrication surfaces can be tailored for specific transport applications. For example, micropatterned arrays of nanopillars can be used to control the direction of liquid spreading by varying the angle of the pillars [16].

1.4.3 Fabrication of Microchannels and Microfluidic devices

There are two major methods for manufacturing microchannels and microfluidic devices. First, is the soft lithography method [17]. This method uses standard IC chip fabrication lithography techniques to create two dimensional moulds in hard polymers. These moulds are used for the rapid fabrication of soft polymer chips. This fabrication method can resolve feature sizes down to 1 µm in the planar directions. Second, microchannels and microfluidic device can be manufactured using micromilling, with features as small as 25 µm and 5 µm resolution. While the resolution is lower than the soft lithography method the time and cost for manufacturing is lower, making this manufacturing method preferable when high resolution is not an issue. Micromilling can be used to create devices in hard substrates such as plastics or metals. It can also be used to create moulds

for soft chip fabrication. Other fabrication techniques include, but are not limited to: hot embossing, nano-injection moulding and nanoimprinting.

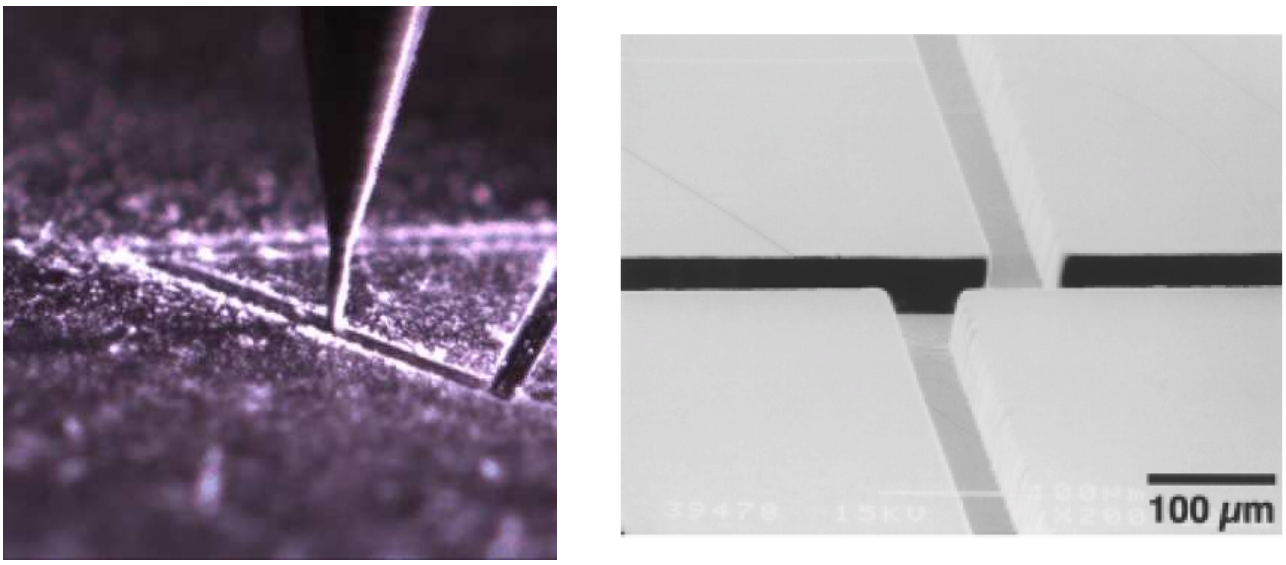

Figure 7. Manufacturing of a hard plastic microfluidic chip via micromilling. The end mill diameter is 100 µm. (left) and a soft polymer chip manufactured using the soft lithography method[17]. (right)

1.5 Outline and objectives

The outline and objectives for this thesis are:

- In Chapter 2 a microfluidic chip is designed and fabricated to generate monodispersed hydrogel microparticles. These microparticles are both biodegradable and mechanically strong. They are made from three precursors that are viscous and reactive. The objective of this work is to show that microfluidics can be used to generate particle from viscous and reactive precursors.
- In Chapter 3 a microchannel heat sink is modified to produce segmented flow of water and air. The heat transfer performance for two-phase flow is measured and compared to single-phase flow. The objective of this work is to show that segmented flow can be generated in a multiple channel heat sink and that this flow will enhance the convective heat transfer.
- In Chapter 4 heterogeneous wettability surfaces are manufactured. This surfaces combine hydrophilic networks with hydrophobic islands. Their pool boiling performance is tested. The objective of this work is to show that heterogeneous wettability surfaces simultaneously enhance heat transfer performance compared to surfaces of homogeneous wettability.

- In Chapter 5 an analytical model to predict the heat transfer coefficient of surfaces with heterogeneous wettability is presented. Models to predict the heat transfer coefficient in pool boiling were developed and have been studied since the 1950's. The objective of this chapter is to show that existing models can be modified for heterogeneous wettability surfaces. This model also provides insight into the physics and a strategy for designing and optimizes heterogeneous wettability surfaces.

2 MICROFLUIDIC FORMATION OF HYDROGEL PARTICLES

2.1 Introduction

Hydrogels are hydrophilic three-dimensional polymer networks, cross-linked chemically and/or physically, capable of retaining a large amount of water. Hydrogel micro particles have applications in drug delivery systems and can be used for biological sensing. The hydrogel particles in this work have a unique composition that makes them both biodegradable and mechanically strong. The MPs are composed of three precusor solutions: partially oxidized dextran (Odext), Teleostean and *N*-carboxyethyl chitosan (CEC). One interesting attribute of the precusor solutions that needs to be considered in design is their high viscosities: 0.347, 0.01 and 0.558 Pas, respectively.

Microfluidic flow focusing has been used to generate MPs with single precursor based (e.g., Ca-alginate), photo-polymerization or one-step reaction systems requiring potentially cytotoxic extraneous cross-linkers or photoinitiator [18-21]. The MPs produced generally have poor mechanical properties [19, 22] rendering them less appealing for certain biomedical applications. Flow focusing using high viscosity fluids has also been demonstrated [23] with a single polymer for the dispersed phase. We designed and tested a microfluidic chip that mixes three viscous precursors and uses flow focusing to generate microparticles that are biodegradable and mechanically strong. The flow rate of the dispersed and the continuous phase where varied to create different size particles. For each trial the particles are characterized by the average size and standard deviation.

2.2 Design of the microfluidic chip

Good mixing between the fluids is important to ensure the manufacturing of quality microspheres. Flow in microchannels is usually laminar due to the low Reynolds number; so that mixing is diffusion-limited. As shown in Figure 8, a y-connection and a 33mm serpentine channel was used to mix the fluids Teleostean and ODext. The serpentine channel was used to increase the mixing length while minimizing the area of the microfluidic chip. The height and width of the serpentine channel, h = 100 μm and w = 500 μm, were chosen so that the pressure drop was less than 2 bar at a filling velocity of 17 mm/s. To estimate the pressure drop we assumed a straight channel with the total length of the serpentine channel, 33 mm. We used the correlation $\Delta p=12\mu LQ/(h^3 w\cdot(1-0.63h/w))$ for channels with rectangular cross-section [2], with the measured viscosity of the most viscous of the two fluid, Teleostean, μ= 0.347 Pas. At low Reynolds number, the turns in the serpentine channel are not expected to significantly increase the pressure drop [24]. The typical time needed to mix the reagents can be estimated as $\tau = (w/2)^2/D$, the diffusion time of Teleostean and Odext across the channel. Assuming $D=1x10^{-9}$ m^2/s, corresponding to the diffusion of 2 Angstroms molecules in water, we obtain τ = 63 s, corresponding to an operation velocity of 0.5mm/s, corresponding to a flow rate of 1.5 μL/min.

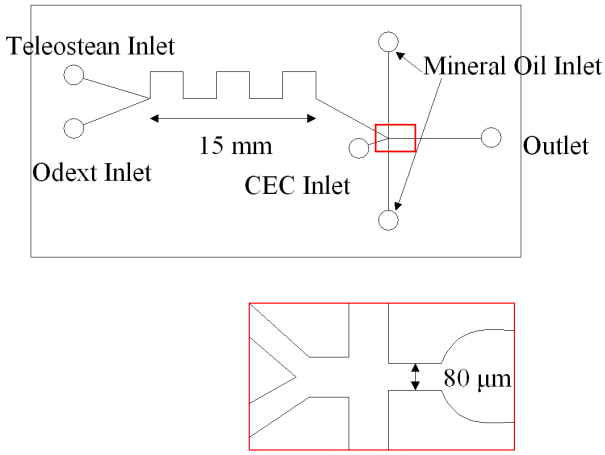

Figure 8: Microfluidic chip design and dimensions

2.3 Experimental set up

The oil phase and precursor solutions were independently infused into the microchannels using a digitally controlled syringe pump (PHD 2000, Harvard Apparatus, Inc., Holliston MA). Odex, Teleostean and CEC solutions were injected separately, as shown in Figure 8, they were mixed to form a uniform stream; this steady stream was broken up by the shearing of the mineral oil flow injected bi-directionally, Figure 8, to form polymer droplet. The droplet were collected in a reservoir, Figure 9, containing 50 ml mineral oil with 0.5 ml of Span-80 added as an emulsifier and allowed to auto-cross-link under constant stirring at 250 rpm (LR400 Lab Stirrer, Yamato, Tokyo, Japan). The reservoir was maintained at 37°C overnight to enable partial dehydration of the MPs formed. Subsequently, the MPs were recovered by precipitation; 60 ml of cold isopropanol was added to the mixture at room temperature while stirring, after 5 min, the mixture was centrifuged (5000 rpm) to separate the organic phase and it was discarded. The residual organic phase was extracted by washing the microspheres three times with approximately

20 ml of an acetone/isopropanol (1:1 ratio) co-solvent mixture. The microspheres were recovered by air-drying overnight at room temperature.

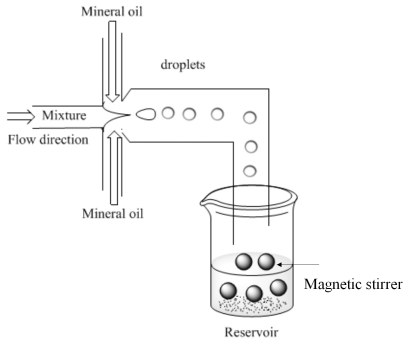

Figure 9: Collection method of microparticles

2.4 Results

The dried MPs were secured on an aluminum stub with copper tape and sputtered with gold; their morphologies were examined by a scanning electron microscope (SEM) (SFEG Leo 1550, AMO GmbH, Aachen, Germany) at 20 kV [3]. The mean size and size distribution of the fabricated MPs were characterized by a dynamic light scattering system (DLS), using a 90 Plus Particle Size Analyzer (Brookhaven Instruments Corporation) at 25 °C with angle detection of 90° for 300 s.

In our experiments the dispersed phase was a mixture of Odext, Teleostean and CEC with a volumetric ratio 2:1:1 respectively. The flow-focusing mechanism generated drops of that precursor fluid in a continuous phase of mineral oil with viscosity μ=0.0276 Pas and density ρ = 840 kg/m^3, with Span 80 as a surfactant. Two syringe pumps were used to drive the dispersed phase and the oil. By optical inspection, we found that the reagents in the droplets generated by the flow focusing process were well mixed.

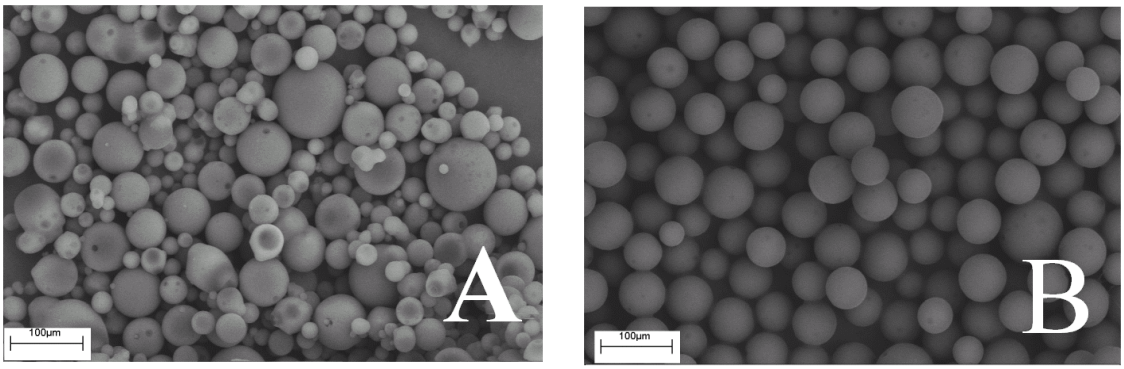

Figure 10: SEM images of microparticles created by A) Traditional emulsion-cross-linking method B) Microfluidic flow focusing.

SEM images of MPs formed by the microfluidic and the traditional method can be seen in Figure 10. A summary of results is shown in Table 1. The MPs manufactured in the microfluidic device had a typical CV < 9%. This is about 4 times better than the CV of 35% obtained in this study by emulsion-cross-linking. While this improvement is sensible, even smaller standard deviations of or below 5% have been reported for particle manufacturing in microfluidic devices [23, 25, 26]. One difference however between these studies and the study described here is the value of the capillary number. The capillary number scales the importance of viscous forces over surface tension forces, and is defined as $Ca = \mu v/\sigma$ where v is defined as the volumetric flow rate divided by the cross-sectional area of the nozzle. In [23], the capillary number of the continuous and dispersed phase was negligible ($Ca \leq 0.1$) so that the drops generated for high viscosity fluids were in squeezing and dripping modes. In our study, assuming an interfacial tension $\sigma = 20$ mN/m and a viscosity $\mu = 0.3$ Pas for the dispersed phase, the capillary number for the continuous and dispersed phase is on the order of 1. Less stable

generation has been reported for capillary number close to one [27]. The high coefficient of variance could also be an effect of the complex and reactive fluid.

Case		A	B	C	D	E
Flow Rate (Oil)	µl/min	250	500	750	500	500
Ca (Oil)		0.72	1.44	2.16	1.44	1.44
Flow rate (P)	µl/min	200	200	200	100	300
Ca (Precusor)		6.25	6.25	6.25	3.13	9.38
Particle size	Mm	50.4	28.5	18.2	18.1	45.6
STD	Mm	4.5	2.0	2.7	1.5	5.0
CV	%	8.9	7.0	14.8	8.3	10.9

Table 1: Summary of results for microparticle generation in a Microfluidic chip (precusor flow given is the total prescribed flow rate of the three fluids)

2.5 Discussion

This work shows that flow focusing can be used to create monodispersed microparticles of a hydrogel. The hydrogel particles generated are biodegradable and mechanically strong making them advantageous for drug delivery applications. The limiting factors on the capillary number of the dispersed phase have also been explored. Since the dispersed phase is viscous there is an upper limit on the flow rate we can achieve before the pressure drop becomes prohibitively high. Conversely, since the fluids are reactive there is a minimum limit to the flow rate so they do not gelatinize in the nozzle. The presents a new set of constraints beyond the balance between shear and surface tension forces that normally drive flow focusing.

3 TWO-PHASE CONVECTIVE HEAT TRANSFER IN MICROCHANNEL HEAT SINKS

3.1 Introduction

The concept of a microchannel heat sink was first introduced by Tuckerman and Pease [4] for the purpose of electronic cooling. As Figure 11 shows, a microchannel heat sink is a device that removes heat, $\dot{Q}$, by fluid flowing in channels over a heated substrate (e.g. a computer chip). Tuckerman and Pease optimized the dimensions of the channels in terms of width and height for single-phase flow of water under the constraint of maximum allowable pressure drop and substrate surface temperature. They found that single-phase water-cooling could remove up to 790 W/cm^2. This heat flux required a mass velocity, *G*, of 5700 kg/m^{2}s and a pressure drop of 220 kPa. A similar optimization process was done by Upadhye and Kandlikar [28] , to minimize the pressure drop under the constraints of a given heat flux and maximum substrate temperature. They found that a water pressure drop below 10 kPa was sufficient to remove 100 W/cm^2 with an optimum channel geometry. One problem with single-phase flow heat transfer in microchannels is the low Nusselt number obtained in laminar flow [29], on the order of 4. Methods for increasing the Nusselt number include: surface area enhancement [30, 31] by geometric obtrusions, tree-like bifurcating channels [32], large aspect ratio channels [4, 33], serpentine channels to promote mixing and turbulence [24], short channels where the entrance region dominates [34, 35], nano-fluids [36, 37], and multiphase flow [30, 33, 38-42].

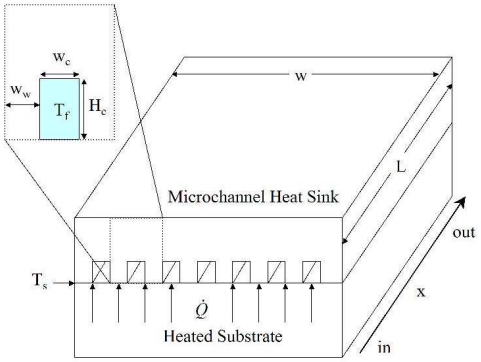

Figure 11: A microchannel heat sink in direct contact with a heated substrate (such as an integrated circuit chip).

There is much interest in multiphase flow because the heat of vaporization is very high. It has been shown [43] that flow boiling can dissipate up to 10,000 W/cm^2 [38, 41], which is 10 times more heat than single-phase flow. While flow boiling is attractive because it delivers high heat flux at the constant temperature of the phase change, it can be difficult to control due to backflow and instabilities. Investigation into controlling the instabilities and backflow include the manufacturing of artificial nucleation sites [44], and inlet restrictions [41, 45, 46]. A drawback of boiling flow, where water is the working fluid, is that the saturation temperature is higher than the operating temperature of most electronics; the proposed solution is to use refrigerants as working fluids since the boiling temperature is lower than water. Refrigerants, however offer lower cooling capabilities due to a lower specific heat and heat of vaporization.

In this work segmented flow is investigated as a way to enhance single-phase heat transfer with water in microchannels. In this work, segmented flow is defined as is a periodic pattern of non-condensable bubbles and liquid slugs created at a T-junction by

the injection of air in liquid-filled microchannels where the bubbles are longer than the channel diameter [47]. More details regarding the physics of the bubble breakup can be found in [7, 47-49]. When surface tension dominates over gravity, which occurs when the Bond number $\rho g d^2/\sigma < 3.368$ [47], recirculating wakes form in the liquid slug. This phenomena has been shown to increases mass transfer [6, 51-53], and is used in chemical engineering to increase mixing [47, 50]. In the work of Kreutzer [6], he also shows that segmented flow can enhance the wall to liquid mass transfer. The transfer of a catalyst from a microchannel wall to the flowing fluid was model numerically and it was found that segmented flow increases the wall to liquid mass transfer 10 times compared to single-phase flow in the laminar regime [6]. These recirculating wakes caused by the presence of segmented flow should also increase heat transfer [6, 54]. It has also been shown that the presence of bubbles increases the pressure drop in the channel due to the Laplace pressure at the liquid gas interface [6, 51], a penalty that needs to be considered.

The presence of bubbles in the system presents an interesting engineering challenge. It may be desired, for industrial applications, to have a closed loop system, where water from the outlet is recirculated through a pump and a heat exchanger to the heat sink inlet; this process might necessitate to remove the air bubbles before the pump and re-inject air after the pump. Bubbles can indeed be removed from segmented flow by the addition of smaller capillary tubes downstream which remove the bubbles due to the difference in interfacial tension [55]. The use of a hydrophobic porous membrane parallel to the channel has also been shown by our group to effectively remove gas bubbles [56].

Further research regarding the removal of the bubbles would be useful for commercial implementation.

3.2 Experimental design based on thermal resistance

In this work, the 1D equivalent resistances method (Figure 12) of Tuckerman and Pease [4] is used to calculate the performance of a micro heat sink (Figure 11). In Figure 12 the total thermal resistance θ_{total} is the ratio of $\Delta T = T_{S,max}-T_{L,in}$, the difference between the maximum heated substrate temperature and the fluid temperature at the inlet, over the power dissipated, $\dot{Q}$.

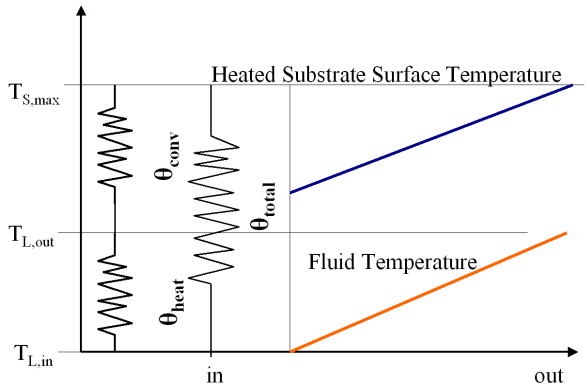

Figure 12: Thermal resistances plotted with the temperature variation for each component for constant heat flux conditions

The total thermal resistance, $\theta_{total} = \theta_{heat} + \theta_{conv}$, is the sum of a heat resistance and a convective resistance. The heat resistance in Eq. 1 is due to the heating of the fluid as it passes through the heat sink; it depends on volumetric flow rate f_L and specific heat capacity of the fluid (c_L).

$$\theta_{heat}=1/(c_L f_L) \quad (1)$$

Equation 2 defines θ_{conv} , which is the resistance of the coolant fluid to heat convection. The expression for θ_{conv} is derived in [4] by treating the rectangular walls of a micro heat sink as fins with adiabatic boundary conditions at their end, the fin efficiency η can be found by $\eta = tanh(mH_c)/mH_c$,where $m = (hP/k_{sub}A_c)^{1/2}$, as given by [4]. In Eq. 2, L_c is the channel length, w is the heat sink width, w_c is the channel width, w_w is the width between the channels, H_c is the channel height and $\alpha = 2H_c/(w_w+w_c)$ is the fin enhancement factor.

$$\theta_{conv}=(2/k_L \mathrm{Nu} L_c w)(w_c/\alpha\eta) \quad (2)$$

From that modeling, the outlet temperature of the fluid and the maximum temperature of the substrate surface can be found based on the power dissipated $\dot{Q}$ and the inlet temperature of the fluid, as shown in Eq. 3 and 4.

$$T_{L,out} = (\dot{Q}\theta_{heat}) + T_{L,in} \quad (3)$$

$$T_{S,\max} = (\dot{Q}\theta_{conv}) + T_{L.out} \quad (4)$$

Several correlations are available for the Nusselt number and pressure drop, as presented below. They will be used to correlate our experiments for the respective single-phase and segmented flow case.

For single-phase, laminar, fully developed flow in rectangular channels with constant heat flux boundary conditions, Nu is calculated according to the correlation in Eq. 5 [29]:

$$\mathrm{Nu}_{\sin} = 8.235(1 - 2.0421(\alpha^*) + 3.0853(\alpha^*)^2 - 2.4765(\alpha^*)^3 + 1.0578(\alpha^*)^4 - 0.1861(\alpha^*)^5) \quad (5)$$

The aspect ratio is characterized by a parameter α^*=min (H, w)/max (H, w). In the case of square channels where $\alpha^* = 1$, this correlation yields Nu = 3.61. The Nusselt number of single phase flow is expected to increase at higher Re due to the increasing thermal entry length. When the thermal entry length is no longer negligible, Nu can be found using a correlation by Lee and Garimella [35]. This correlation is valid for rectangular

channels of any aspect ratio, constant heat flux boundary conditions, and laminar, hydrodynamically developed flow. When the hydrodynamic entry region is no longer negligible, correlations by Muzychka and Yovanovich [57] can be used to find Nu. Their work is valid for Pr > 0.1, uniform heat flux and constant surface temperature, and any channel cross-sections.

The pressure drop for single-phase flow is found using the Churchill correlation valid for both laminar and turbulent flow [58], given in Eq. 6, where d is the hydraulic diameter, K is the minor loss term and U_L is the liquid velocity.

$$\Delta p = \rho\,(4f_r L_c/d + K)U_L^2/2 \tag{6}$$

For segmented flow, Nu at constant heat flux was estimated with a correlation established from detailed multiphase flow simulations in cylindrical pipes by Lakehal et al. [52].

$$\mathrm{Nu}_{seg} = \mathrm{Nu}_{sin} + 0.022\,\mathrm{Pr}^{0.4}\,\mathrm{Re}_{seg}^{\,4/5} \tag{7}$$

In Eq. 7, Nu_{sin} is the Nusselt number for single-phase fully developed liquid flow, found with Eq. 5, Pr is based on the properties of the liquid phase, and $\mathrm{Re}_{seg} = d\,\rho_L U_B/\mu_L \cdot (L_B/(L_B+L_{slug}))$, where U_B is the bubble velocity and the definitions of L_B and L_{slug} are the respective length of the bubble and liquid slug, as shown in Figure 13-Figure 15. Note that this definition is equivalent to the Reynolds number proposed in [52]. Equation 7 is valid for well-defined gas bubbles when d is on the order of mm, Pr > 1, Re_{seg} is on

the order of 1000, and 300 K < $(T_L)_{mean}$ < 340 K. Multiphase flow simulations in [52] revealed two mechanisms that increase Nu: the generation of the bubbles and the circulation in the liquid slugs. As mentioned in section 3.1, a segmented flow with recirculating wakes can be generated provided the Bond number $\rho g d^2/\sigma$ < 3.368 [6, 47] and the capillary number Ca<0.04 [6].

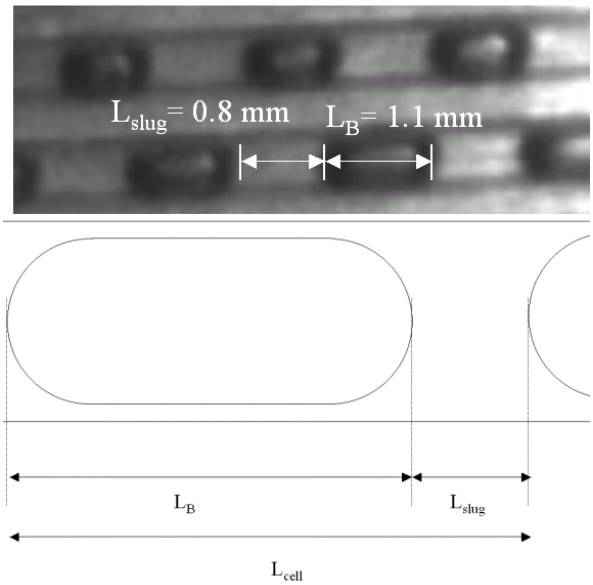

Figure 13: Definition of L_B, L_{slug}, L_{cell} and values for segmented flow at G_L = 670 kg/m^{2}s

Other correlations for determining the Nusselt number of segmented flow were examined. As mentioned in section 3.1, Kreutzer [6] obtained an expression for Nu from numerical simulation in square channels. Kreutzer's correlation is only valid when there is full circulation in the slugs and was only verified for Re < 300. Hetsroni et al. [59] conducted the first experimental work on the heat transfer of gas-liquid flow in microchannel heat sinks. They established correlations for the Nusselt number in triangular channels, valid for negligible entry length and Re < 100. In this work, we use

the correlation of Lakehal et al. [52], which best reflects our experimental conditions in terms of Re and Ca range, flow patterns and entry length.

The pressure drop in segmented flow can be described with Eq. 8 [51], where a pressure drop term across the bubbles is added to the single-phase pressure drop for the liquid slugs. The pressure drop depends on two measurable quantities: the number of bubbles in a channel, *n*, and slug length, L_{slug} [51], as per Eq. 8.

$$\Delta p = n\left(\frac{U_B \mu}{d}\right)\left[\frac{B}{2}\left(\frac{L_{slug}}{d}\right) + C(3)^{2/3}(\mathrm{Ca})^{-1/3}\right] \tag{8}$$

For square channels the hydraulic coefficient, B = 56.91 and the gas constant C = 2.39, as determined by [60]. The capillary number, Ca, is determined by the bubble velocity [6, 54, 61].

$$\mathrm{Ca} = U_B \mu_L / \sigma \tag{9}$$

Parameters in Eq. 7-9 such as L_{slug}, L_B and U_B, are available from high-speed visualizations in our experiments so that the experimental values of pressure drop and Nu can be compared with the correlations.

We also used Eq. 7-9 to design the microchannel heat sink. In the design process, the bubble velocity is not known, and we propose the following process to determine U_B from an assumed water mass velocity G_L. We first assume a liquid volume fraction, ε = 0.5, and slug length Ls = 0.001 m, which are representative of our experiments as shown in Figure 13. Assuming that the cross-section of the bubble is constant along its length, the bubble velocity is expressed by mass conservation [6, 53, 54].

$$U_B/U_{slug}=A_c/A_B \quad (10)$$

With the slug velocity defined as $U_{slug}= G_L/\varepsilon\rho_L$ we obtain:

$$U_B=A_cG_L/(A_B\,\varepsilon\rho_L) \quad (11)$$

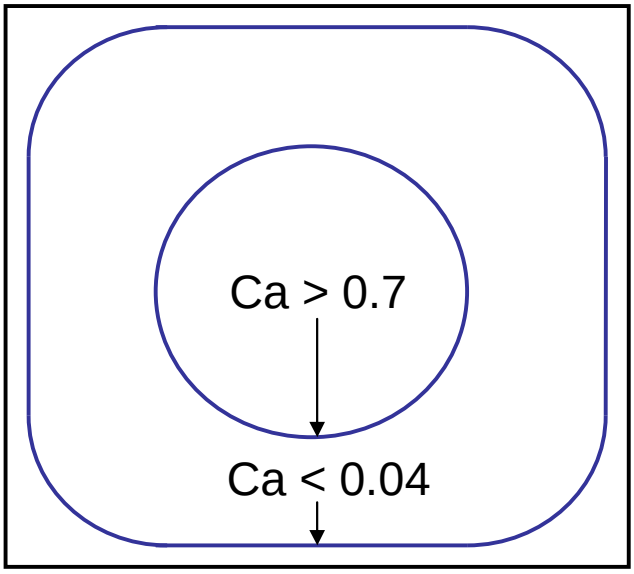

Figure 14. Cross-sectional view of a bubble in a square channel at low and high capillary values[6].

In Eq. 11 the only unknown parameter is the cross-sectional area of the bubble, A_B, which can be found as follows. Figure 14 shows the typical cross-sectional shape of the bubble for Ca < 0.04 [6]. Assuming a cross-section shape as in Figure 14, with a thin, constant film thickness δ along the walls and a thicker film at the edges with radius of curvature, $r = (w_c-2\delta)/4$, the bubble area can be calculated by dividing the cross-section of the bubble into several contiguous subsections, where $4A_1 = \pi(w_c-2\delta)^2/16$, $4A_2 = (w_c-2\delta)^2/2$ and $A_3 = (w_c-2\delta)^2/4$ and the total bubble area is $A_B =4A_1+ 4A_2+ A_3$. The film thickness δ is a function of the capillary number and is expressed by Eqs. 12 and 13 using a correlation based on the simulations of Hazel and Heil [61].

$$\delta = 0.00332 w_c \qquad \text{For } 0.001 < Ca < 0.04 \tag{12}$$

$$\delta = -0.0423e^{(-Ca/5.3092)} - 0.1018e^{(-Ca/0.3343)} + 0.1761 \qquad \text{For Ca} > 0.04 \tag{13}$$

3.3 Design

A microchannel heat sink was designed in our laboratory to best demonstrate how segmented flow can enhance Nu in comparison with single-phase flow. Considering Figure 12, the heat transfer enhancement is most noticeable under two conditions: first, θ_{conv} dominates over θ_{heat} , and second, the flow regime is such that there is a large difference between θ_{conv} for segmented and θ_{conv} for single-phase flow. For design purposes, we have plotted Eq. 1 and 2 in Figure 15-17, to show how the thermal resistances vary with liquid flow rate for typical channel diameters, with the same base area, L= 0.025 m and w=0.0075 m and $w_w = w_c$. The Ca transition represents the point where Ca = 0.04, when the bubble cross-section changes from the non-axisymmetric shape shown in Figure 14 to a more circular cross-section, which results in a dramatic decrease of circulation in the slug [6, 52, 62]. The Re transition represents the change from laminar to turbulent flow for the liquid flow rate. For 500 μm wide channels, Figure 15 shows that the Reynolds number of the liquid flow must be greater than 60 in order to be in a regime where θ_{conv} dominates over θ_{heat}. Figure 16 and Figure 17 show the thermal resistances plotted for different channel widths, with the length remaining unchanged. For smaller geometries, such as 50 μm, shown in Figure 16, θ_{heat} is the dominant resistance so that changes in Nu would not significantly modify the surface temperature, which is used to experimentally determine the Nusselt number. For larger

widths, such as 2 mm, shown in Figure 17, values of θ_{conv} are much higher than in the 500 μm microchannel case, resulting in a less efficient heat sink.

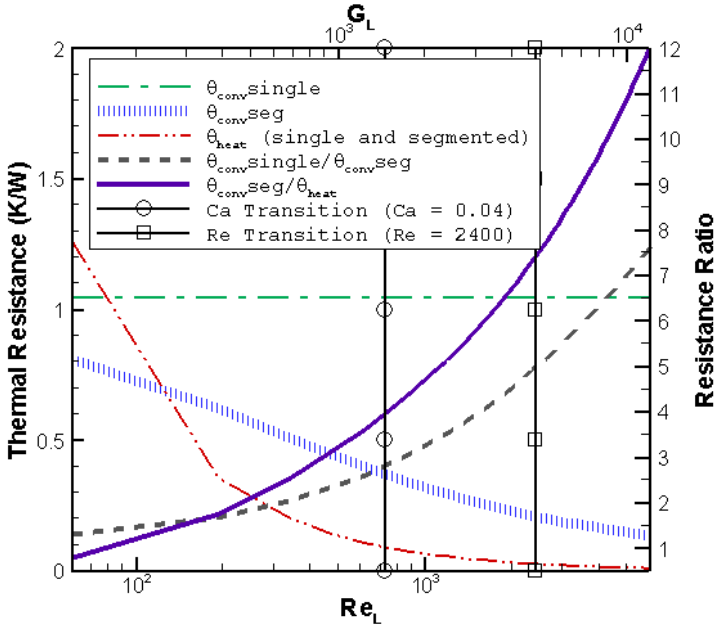

Figure 15: Thermal resistance plotted for a microchannel heat sink with 7 parallel 500 μm channels, 25 mm in length

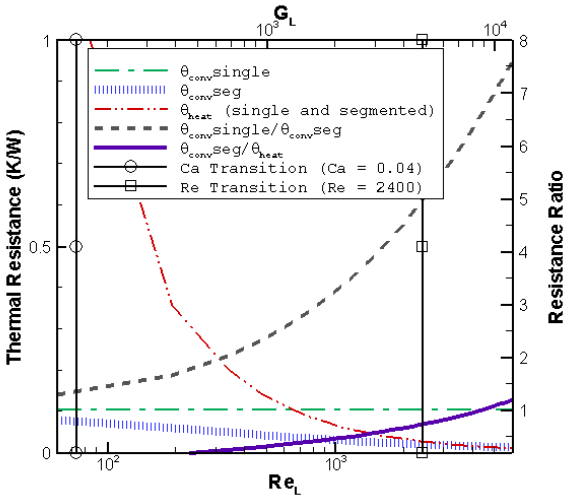

Figure 16: Thermal resistances plotted for a microchannel heat sink with 70 parallel 50μm channels, 25 mm in length

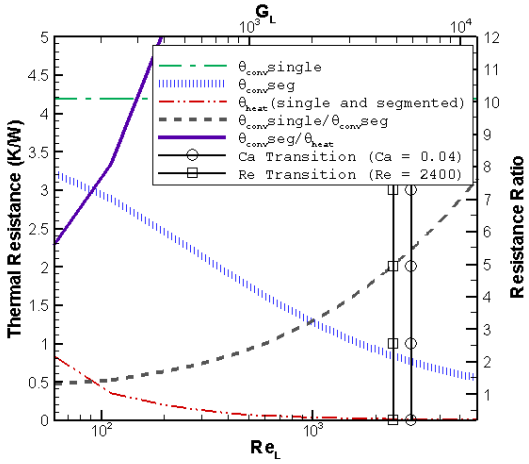

Figure 17: Thermal resistances plotted for a mini channel heat sink with 3 parallel 2mm channels, 25 mm in length

3.4 Fabrication and experimental set up

The microchannel heat sink and heated substrate are shown in Figure 18. The heated substrate, made from aluminum, was designed to provide uniform heat flow. Before the single-phase and segmented flow measurements, a simple experiment was performed to quantify the heat loss of the heated aluminum block through the insulation, and verify that the surface temperature of the substrate can be found using a linear interpolation of the thermocouple measurements. The polycarbonate microchannnel heat sink was removed, so that the top surface of the aluminum block is exposed to air. The rest of the substrate is insulated with melamine foam approximately 2 cm thick, as shown in Figure 19. An infrared pyrometer was used to measure the substrate temperature. Since the emissivity of aluminum is very low, 0.05, the surface of aluminum was painted black so that the emissivity was in the range of the pyrometer (a value of 0.95 was chosen). The

natural convection heat transfer *h* was obtained by a correlation specific to small geometries and dependent on surface temperature, ranging from 15-25 W/m^{2}K [63]. Five rows of three K-type thermocouples, as shown in Figure 18b, were used to determine the surface temperature and temperature gradient using linear extrapolation. The test was run at 5 substrate temperatures: 50, 75, 90, 115, 150˚C .The maximum heat loss through the insulation $\dot{Q}_{loss}$ (see equation in Figure 19) was found to be less than 1W, which is negligible compared to the 40 W heat flux we apply during measurements involving fluid flow. The surface temperature was measured with a pyrometer and was found to correspond within 0.5˚C to the surface temperatures extrapolated from the set of 5 thermocouple measurements perpendicular to the surface. The standard deviation of the extrapolated values along the surface was less than 0.5˚C.

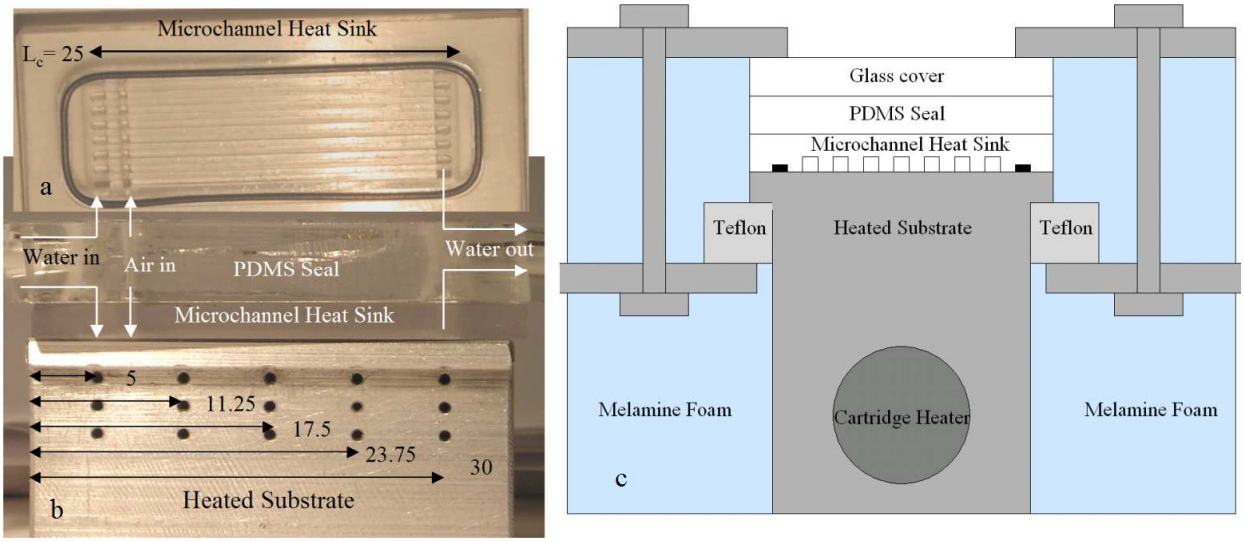

Figure 18: a) Typical segmented flow in our microchannel heat sink at 860 kg/m^{2}s b) Microchannel heat sink with o-ring bc) Test section –-heated substrate with showing thermocouple locations, with microchannel heat sink on top (all units are mm) c) Cross-sectional view of test section

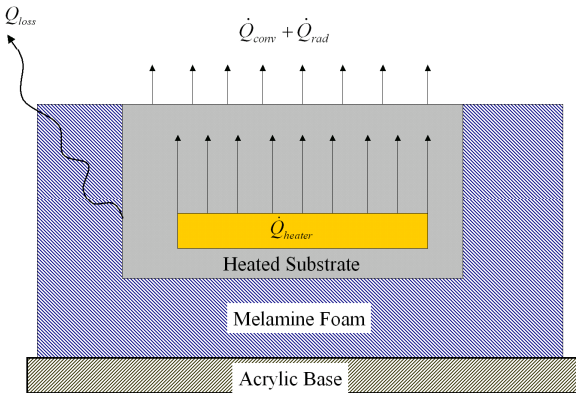

Governing Equations

$$\dot{Q}_{heater} = \dot{Q}_{conv} + \dot{Q}_{rad} + \dot{Q}_{loss}$$

$$\dot{Q}_{conv} = hA_s(T_s - T_\infty)$$

$$\dot{Q}_{rad} = A_S \varepsilon\sigma \ (T_s^4 - T_\infty^4)$$

Figure 19: Set up of heated substrate for energy balance verification

The microchannel heat sink (Figure 18a) was milled from a polycarbonate slab, with a glass transition temperature of 150˚C, into seven parallel square channels with respective length and width of 25 mm and 500 µm. Polycarbonate was used since it is transparent and easy to manufacture. The heat sink was pressed on top of the heated substrate and sealed with an O-ring. It was heated with a constant power of 40W and the water flow rate was varied from 238 – 3095 kg/m^{2}s. Figure 18 shows the experimental set up for the single-phase and segmented flow experiments.

The heated substrate and microchannel heat sink were insulated with melamine foam, as shown in Figure 18c, with a typical loss measured as less than 1W. The water was pumped with a peristaltic pump, and the liquid mass velocity G_L was found by measuring the fluid volume at the outlet over time. Bubbles were generated by injecting air through a slit at constant pressure using a Druck DPI 530 pressure regulator. The pressure was varied depending on G_L to produce a liquid fraction close to 0.5. The pressure drop along the channel was measured with a pressure transducer (Honeywell, 15 psi/105.53 kPa, ± 0.087 psi / 0.61 kPa uncertainty, 100 µs response time). Thermocouples (Type K, 0.5 mm

diameter, Omega, 100ms response time, ± 0.5˚C uncertainty) recorded inlet and outlet temperatures of the fluid, along with 15 measurements on the substrate, as shown in Figure 18b.

3.5 Nusselt number calculations

The final goal of these measurements is to calculate the average convection coefficient and Nusselt number, in order to compare the improvement in heat transfer from single-phase to two-phase flow. An energy balance is solved for both a unit cell along the width of the channel and for a differential element along the length of the channel, Figure 20.

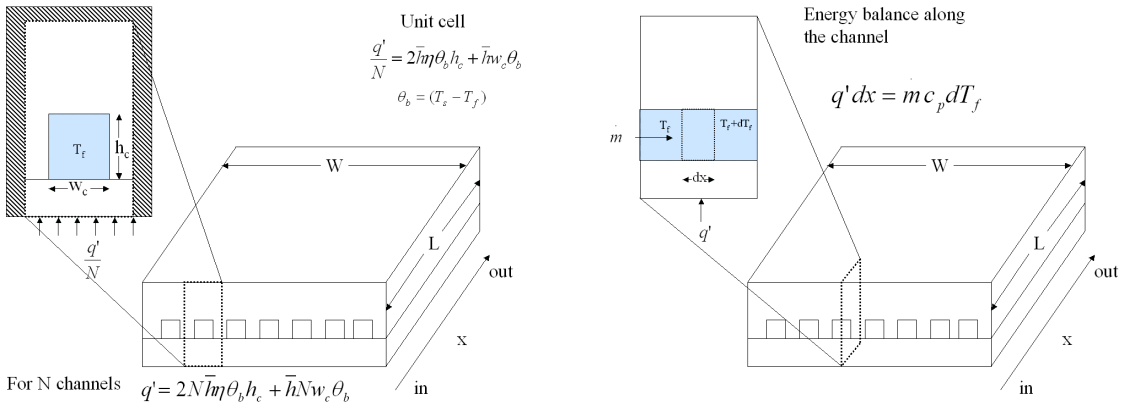

Figure 20: Energy balance for unit cell and along the length of the channel

From the energy balance along the length of the channel, it is found that

$$\frac{dT_f}{dx} = \frac{q'}{\dot{m}c_p} \tag{14}$$

Substituting in the value found for q' along the width of the channel and you obtain

$$\frac{dT_m}{dx} = \frac{(2\eta h_c + w_c)N\bar{h}\theta_b}{\dot{m}c_p} \tag{15}$$

where $\theta_b = (T_s - T_f)$ and $\eta = \frac{\tanh(mh_c)}{mh_c}$ and $m = \sqrt{\frac{\bar{h}}{k_s w_w}}$

Rearranging the equation and integrating on both sides the equation becomes

$$\dot{m} c_p \Delta T_f = \int_0^L (2\eta h_c + w_c) N \bar{h} \theta_b dx \tag{16}$$

Since the equation is to find the average convection coefficient, which is a constant, $\bar{h}$ and all the geometric constants can be removed from the integrand

$$\dot{m} c_p \Delta T_f = (2\eta h_c + w_c) N \bar{h} \int_0^L \theta_b dx \tag{17}$$

In order to solve this integral the trapezoidal rule is used to numerically integrate.

$$\int_0^L \theta_b dx = \sum_1^4 [\Delta x (\frac{\theta_{b,i}}{2} + \frac{\theta_{b,i+1}}{2})] \tag{18}$$

Δx is the distance between two rows of thermocouples, 0.00625m. Since the numeric integration is based on four quadrants (five points), it is simple to write the full solution.

$$\sum_1^4 [\Delta x (\frac{\theta_{b,i}}{2} + \frac{\theta_{b,i+1}}{2})] = \tag{19}$$

$$\Delta x [(\frac{T_{s,a}}{2} + T_{s,b} + T_{s,c} + T_{s,d} + \frac{T_{s,e}}{2}) - (\frac{T_{f,in}}{2} + T_{f,b} + T_{f,c} + T_{f,d} + \frac{T_{f,out}}{2})]$$

However, this equation cannot be solved since the values of T_f are unknown at points: b, c and d. Since a constant heat flux is applied to the substrate, the temperature of the fluid along the channel is expected to vary linearly [64]. The expected variation of the fluid and substrate temperature, along with the estimate fluid temperature is shown in Figure 21.

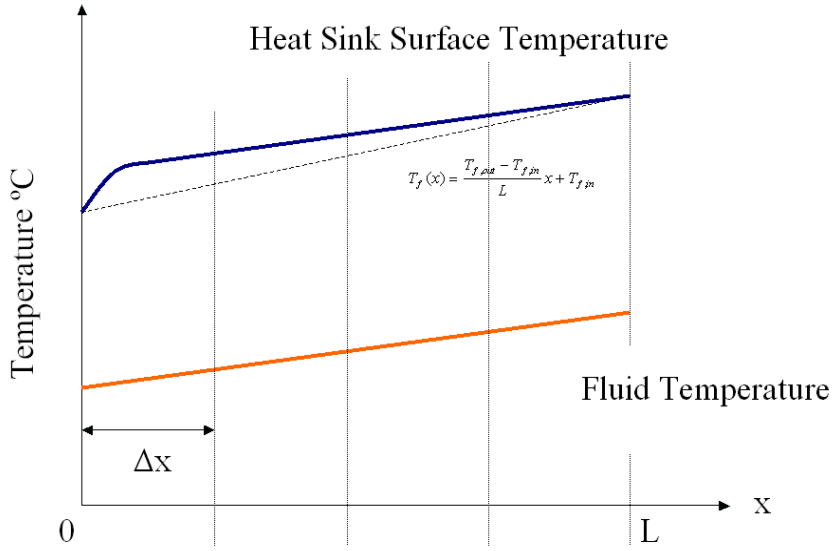

Figure 21: Expected variation of fluid and surface temperature along the length on the channel.

The equation for estimating the fluid temperature can be solved for the specific value needed and can be substituted back into equation 19.

$$T_f(x) = \frac{T_{f,out} - T_{f,in}}{L} x + T_{f,in} \tag{20}$$

$$T_{f,b} + T_{f,c} + T_{f,d} = \frac{T_{f,out} - T_{f,in}}{L}(.00625 + .0125 + .01875) + T_{f,in} \tag{21}$$

$$\sum_{1}^{4}[\Delta x(\frac{\theta_{b,i}}{2} + \frac{\theta_{b,i+1}}{2})] = \tag{22}$$

$$\Delta x[(\frac{T_{s,a}}{2} + T_{s,b} + T_{s,c} + T_{s,d} + \frac{T_{s,e}}{2}) - (\frac{3T_{f,in}}{2} + \frac{.0375(T_{f,out} - T_{f,in})}{L} + \frac{T_{f,out}}{2})]$$

The numerical integration is now based on the five surface temperatures and the inlet and outlet temperature of the fluid, which are all known from experimental data. The integral can be substituted back into equation 17 and rearranged to solve for $\bar{h}$.

$$\bar{h} = \dot{m} c_p \Delta T / \{(2\eta h_c + w_c) N \Delta x[(\frac{T_{s,a}}{2} + T_{s,b} + T_{s,c} + T_{s,d} + \frac{T_{s,e}}{2}) - (\frac{3T_{f,in}}{2} + \frac{.0375(T_{f,out} - T_{f,in})}{L} + \frac{T_{f,out}}{2})]\} \quad (23)$$

The convection coefficient can also be used to find the Nusselt number, $Nu = \frac{\bar{h}d}{k}$.

3.6 Experimental results

The convective heat transfer measurements were made using the heat sink described in the previous section at constant heating power of 40W, and with water flow rates between 35-300 mL/min, corresponding to water mass velocities G_L of 300-3000 kg/m^{2}s and Re_L from 160-1580, where Re_L is defined as $G_L d/\mu_L$ for both single phase and segmented flow. Neglecting the low thermal losses through the insulation, as discussed in section 3.3, the enthalpy change of the fluid can be replaced by the power supplied by the heater. An energy balance surrounding the channel provides the convection coefficient, h, as detailed in section 3.5.

$$\dot{Q}_{heater} = (2\eta H_c + w_c) N h \int_0^L \beta \, dx \quad (24)$$

Where β, η and N are the temperature difference between the substrate and the fluid, the fin efficiency and the number of channels, respectively [33].

The Nusselt number is found from the heat transfer coefficient by Nu = hd/k_L, where k_L = 0.64 W/Km is the fluid thermal conductivity. The maximum uncertainty of the Nusselt number is ± 4 % due to the propagation of uncertainties in the temperature, geometry and thermal losses through the insulation. A summary of all uncertainties and their sources can be found in Table 2. Major contributors to the uncertainty are the thermocouple

measurements and the heat flow measurement. For example, at G_L = 1140 kg/m^{2}s, the average temperature difference β is 20˚C with an uncertainty of ± 0.5˚C, or ± 2.5 %. Also, section 3.3 showed that the uncertainty of $\dot{Q}_{heater}$ due to heat losses is less than 1 W, i.e. 2.5 %.

Variable	Maximum uncertainty by percent	Maximum uncertainty absolute	Source
Pressure	± 32 %± 0.61 kPa	± 0.61 kPa	Manufacturers Specs (Honeywell)
Temperature	± 2.2 %± 0.5°C	± 0.5°C	Manufacturers Specs (Omega)
Heat Flow	2.5 %1 W	1 W	MaximumH heat lost through insulation
Volumetric flow rate	0.8 %0.2 mL/min	0.2 mL/min	Resolution limit
Channel dimensions	± 1 %± 5 μm	± 5 μm	Resolution limit
Nusselt number	± 4 %	± 0.504	Calculated by uncertainty propagation [65]

Table 2: Uncertainty analysis, measured uncertainties, and uncertainty on the Nusselt number.

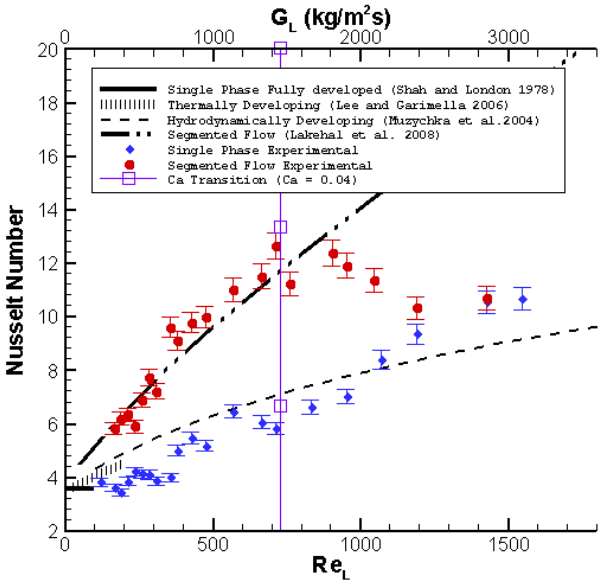

Figure 22: Theoretical and measured values of Nusselt number for single phase and segmented flow versus the prescribed Reynolds number and mass velocity of water.

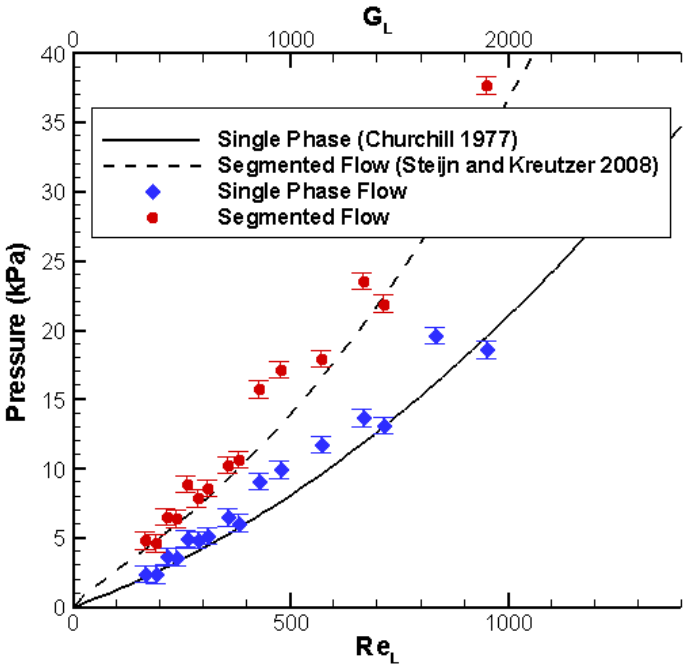

Figure 23: Theoretical and measured values of pressure drop for single phase and segmented flow.

Figure 22 shows that segmented flow increases the dimensionless heat transfer coefficient Nu up to 140% over single phase flow, for values of G_L < 2000 kg/m^{2}s, in very good agreement with the numerically obtained correlation of [52]. For flow rates higher than 2000 kg/m^{2}s (or Re_L~1000), the heat transfer enhancement due to the segmented air bubble flow decreases quickly, and at G_L > 2500 kg/m^{2}s (Re=1200), the bubbles have no more influence on the heat transfer process. Interestingly, this transition starts at flow rates where the capillary number reaches the transition value of 0.04 (shown by a vertical bar), and the flow visualizations in Table 3 confirm a transition to churn flow. This might indicate that segmented flow enhances heat transfer provided the film between bubbles and wall does not become too thick, which would weaken the recirculation wakes, as explained in section 3.3 and in [6, 7, 53, 54]. As a side note, we were only able to produce segmented flow for values of G_L between 330 and 2850 kg/m^{2}s. At lower G_L values segmented flow is replaced by bubbly flow (i.e. bubbles with diameters smaller than the channel diameter), and at higher G_L values a churn flow appears (fast bubbles with thick films, Ca reaching 0.04 and above, no heat transfer enhancement), in agreement with the data compiled by [3, 47]. Visualization of these flow regimes can be seen in Table 3. The increasing values of the Nusselt numbers for single phase flow at larger flow rates are very likely due to the non-negligible thermal and hydrodynamic entry lengths. As mentioned in section 3.2, the correlations of Lee and Garimella [35] can be used to calculate Nu for thermally developing flow. In our experiments the thermal entry region accounts for 10% of the channel length at Re = 30. This correlation is only valid until Re ~100, when the hydrodynamic entry becomes non-

negligible. For cases where both thermal and hydrodynamic entry length are significant, the correlation of Muzychka and Yovanovich [57] should be used. Predictions from this correlation agreed very well with our experimental values for Re >100 [57].

Case	**a**	**B**	**C**	**d**
G_L (kg/m^{2}s)	238.08	380.95	1333.33	3095
Flow Regime	bubbly	Slug	Slug	churn
Average L_B (mm)	0.34	1.16	1.04	1.08
Average L_{slug} (mm)		0.93	0.79	
E		0.482	0.47	
Increase in Δp (kPa)		2.26	9.81	
3.6.1 Visualization	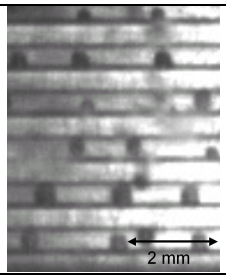	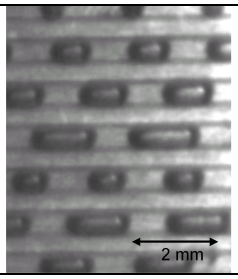	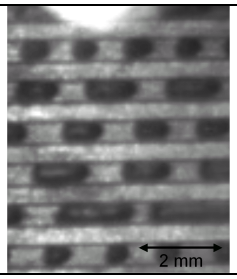	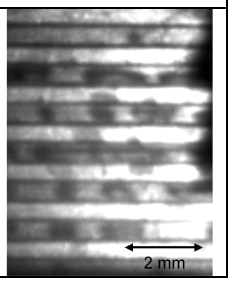

Table 3: Visualization of four trials spanning three flow regimes with corresponding liquid mass velocity. The liquid fraction, ε, can only be calculated for slug flow using the method described in section 3.2. In case d the low picture quality is due to the limited frame rate of the camera.

The penalty in pressure drop associated with segmented flow is evaluated in Figure 23, which shows that segmented flow exhibits pressure drops higher than single phase flow at the same prescribed liquid mass velocity, as predicted by the correlations in [51] .The segmented flow heat transfer enhancement scheme that we present here would only be of interest if it provides a higher Nusselt number than single phase flow, for the same pressure drop.

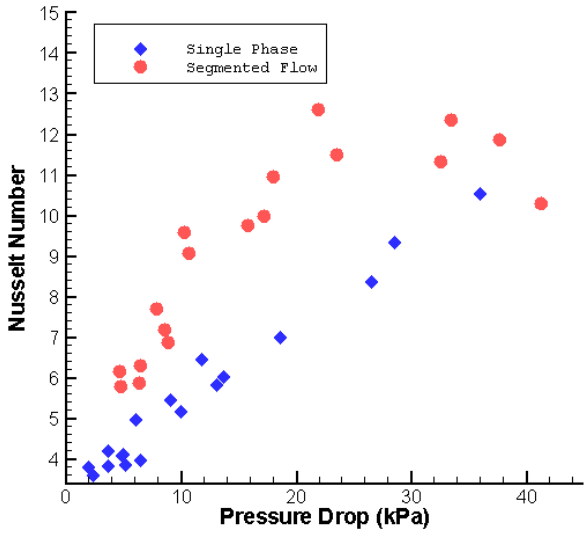

Figure 24: Pressure drop for single phase and segmented flow compared to the Nusselt number.

This is verified in Figure 24 for pressure drop values ranging from 5 to 30 kPa, where the Nusselt number enhancement is about 50% using segmented flow rather than single phase flow, for the same amount of pressure drop. This heat transfer enhancement is also seen with the lower measured substrate temperature shown in Figure 25. Incidentally, Figure 25 confirms that the temperature variation along the substrate increases linearly: this was expected since the fluid experiences a constant heat flux.

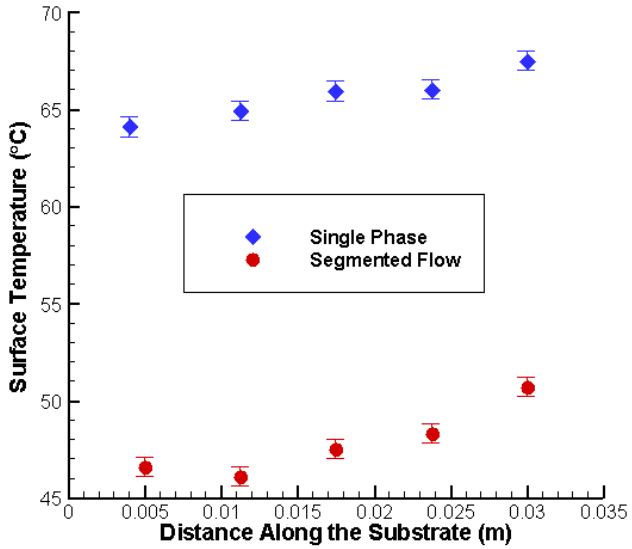

Figure 25: Example for the variation of the surface temperature, T_s, along the substrate for comparison of single-phase and segmented flow

In table 4 the pressure drop and Nusselt number of our segmented flow experiments are compared to single phase and evaporative flow measurements with similar flow rate and heat flux. The flow boiling results are from the work of Qu and Mudawar [33, 42], produced by an aluminum microchannel heat sink with 21 channels and a hydraulic diameter of 348.8 μm. Table 4 shows that segmented flow provides Nusselt number values in a range that is between single-phase and evaporative cooling.

Regime	G (kg/m^2s)	q" (W/cm^2)	Pressure Drop (kPa)	Nusselt
Single phase (this work)	238-3095	21	1.9-28.5	3.4-10.7
Segmented flow (this work)	333-2857	21	4.58-41.2	5.8-12.6
Boiling Flow [76,176]]	135-402	25-130	0.5-20	10.1-22.9

Table 4. Comparison of three flow regimes

3.7 Discussion

Experiments and optimization studies have demonstrated that segmented flow could enhance heat transfer by up to 140% in a microchannel heat sink, in comparison with single-phase flow at the same liquid flow rate. The Nusselt number was used to characterize the improvement in heat transfer. Also, the pressure drop penalty in implementing segmented flow was reasonable, in the sense that for the same values of pressure drop segmented flow delivers a higher Nusselt number than single phase flow. We determined that segmented flow would provide an intermediate step between single-phase and boiling flow for the purpose of electronic cooling. Also, we measured that the heat transfer enhancement only occurs for flow rates and capillary numbers that actually generate segmented flows. At lower or higher capillary numbers, we explain that no significant heat transfer enhancement is observed because segmented flow is replaced by bubbly or churn flow respectively.

4 SURFACES OF HETEROGENEOUS WETTABILITY FOR ENHANCED POOL BOILING

4.1 Introduction

Boiling is an efficient process to transfer large amounts of heat at a prescribed temperature because of the large latent heat of vaporization. The term *flow* boiling describes the boiling of liquids forced to move along hot surfaces, while in *pool* boiling, the topic handled in this paper, the liquid is stagnant and in contact with a hot solid surface [66]. Besides the common experience of boiling water in an electric kettle, pool boiling has applications in metallurgy, high performance heat exchangers, and immersion cooling of electronics. Pool boiling performance is measured with two parameters, the heat transfer coefficient (HTC) and the critical heat flux (CHF). The CHF is measured by increasing the surface temperature until a transition from high HTC to very low HTC occurs, which signifies the formation of a vapor film insulating the liquid from the heated surface, a phenomenon called dry out.

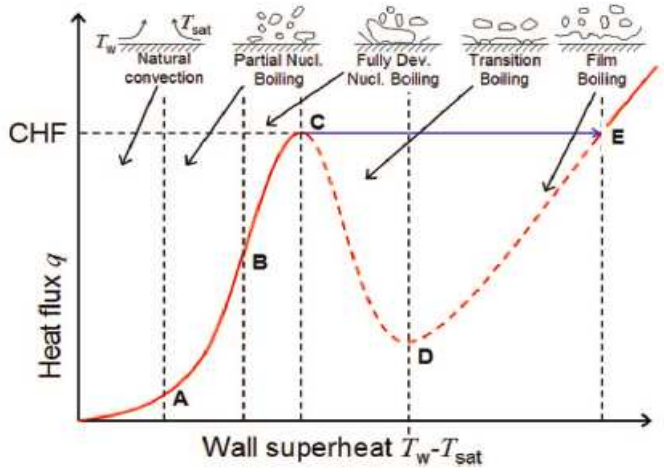

Figure 26: Typical pool boiling curve with description of the various boiling regimes. Image is taken from [67].

Several characteristics determine the performance of a boiling surface. First, nucleation sites in appropriate number and dimensions need to be provided such as cavities, rough areas or hydrophobic islands [68]. As of today, the performance of boiling surfaces has been increased using four approaches: by increasing the number of nucleation sites or cavities [69], by using wicking structures to prevent dry out [70], by increasing the surface area with fins or fluidized bed [70-73], and by enhancing the wettability of the surface [72-74]. The latter objective is justified by experiments of Wang and Dhir [75], showing that the critical heat flux was increased by enhancing surface wettability. Wettability can be enhanced by either increasing the surface roughness or with microstructure or nanostructure coatings. For instance, Jones et al. [76] have shown that a well chosen roughness can double or triple the heat transfer coefficient. Significant heat transfer enhancement has also been obtained with surfaces coated with a µm-thick carpet of nanometer diameter rods (nanorods) [72, 73]. The CHF enhancement was attributed to

coupled effects such as the availability of a range of nucleation sites [72] and the superhydrophilicity of the nanowire arrays [73].

A common assumption in boiling studies typically [66] is that the surface has a unique value of wettability. However the above introduction shows that the influence of wettability on boiling is complex: while hydrophobic zones promotes nucleation, the surface hydrophilicity does enhance the CHF [75]. In this work microlithography techniques are used to design surfaces combining hydrophobic and hydrophilic zones, for pool boiling experiments. The intuition is that a well-design network of hydrophobic and hydrophilic might promote nucleation, enhance the heat transfer coefficient, and even prevent dry out and increase the critical heat flux.

4.2 Design and fabrication of surfaces

Several patterns have been designed and fabricated using photolithography as shown in Figure 27, with hydrophobic and hydrophilic zones. The pattern size *d* was typically between 40 and 60% of the pitch p between patterns. Pattern shapes were hexagonal. We varied the pitch p from 50 to 200 µm, as well as the connectivity of the hydrophobic and hydrophilic patterns. Hydrophilic surfaces with hydrophobic islands were called *hydrophilic networks*, and noted *(+)*, meaning that any two hydrophilic zones could be joined without passing over a hydrophobic zone. Hydrophobic surfaces with hydrophilic islands were called *hydrophobic networks*, and noted *(-)*.

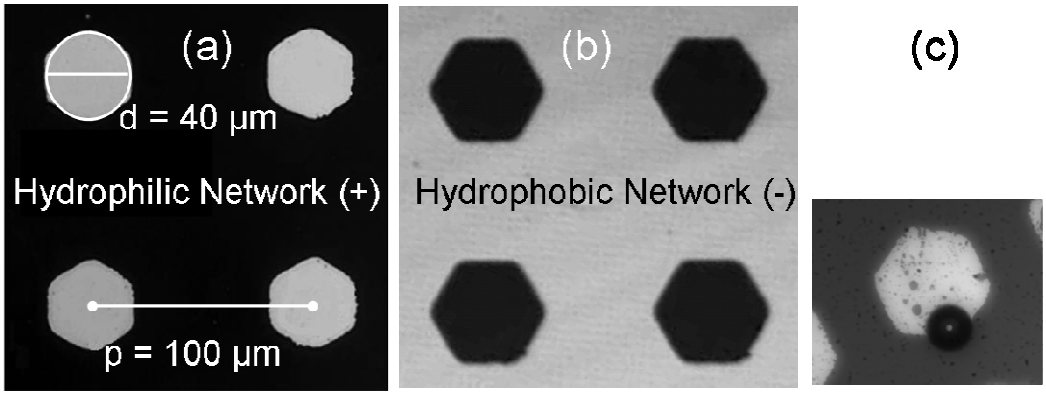

Figure 27: Typical micrographs (a,b) of surfaces with hydrophilic (black) and hydrophobic (grey) zones. The pattern diameter d is the diameter of the inscribed disk. The pattern pitch is p. Surface (a) is hydrophilic with hydrophobic islands, called a hydrophilic network, and noted (+). Surface (b) is hydrophobic with hydrophilic islands, called hydrophobic networks, and noted (-). At low superheat, bubbles typically nucleate at the interface between areas of different wettability (c).

The patterns were produced with a photolithographic process. First, the oxidized two-sided polished silicon wafer is coated with a 25nm Aluminum layer. Then, a hydrophobic coating of Teflon (AF400, Dupont), diluted in Fluorinert (FC-40) at a 1:3 ratio, is spun on top of the Aluminum layer to a thickness of about 100 nm. After baking at 90°C for 20 minutes, 1µm layer of positive photoresist (S1818, Shipley) is spun on top of the Teflon. The wafer is then exposed to 180 mJ/cm^2 of UV light using a transparency mask. The exposed area and the underlying Teflon and Aluminum are then removed using oxygen plasma and a developer (300 MIF, AZ Electronic Materials). Finally, the remaining positive photoresist is removed with acetone.

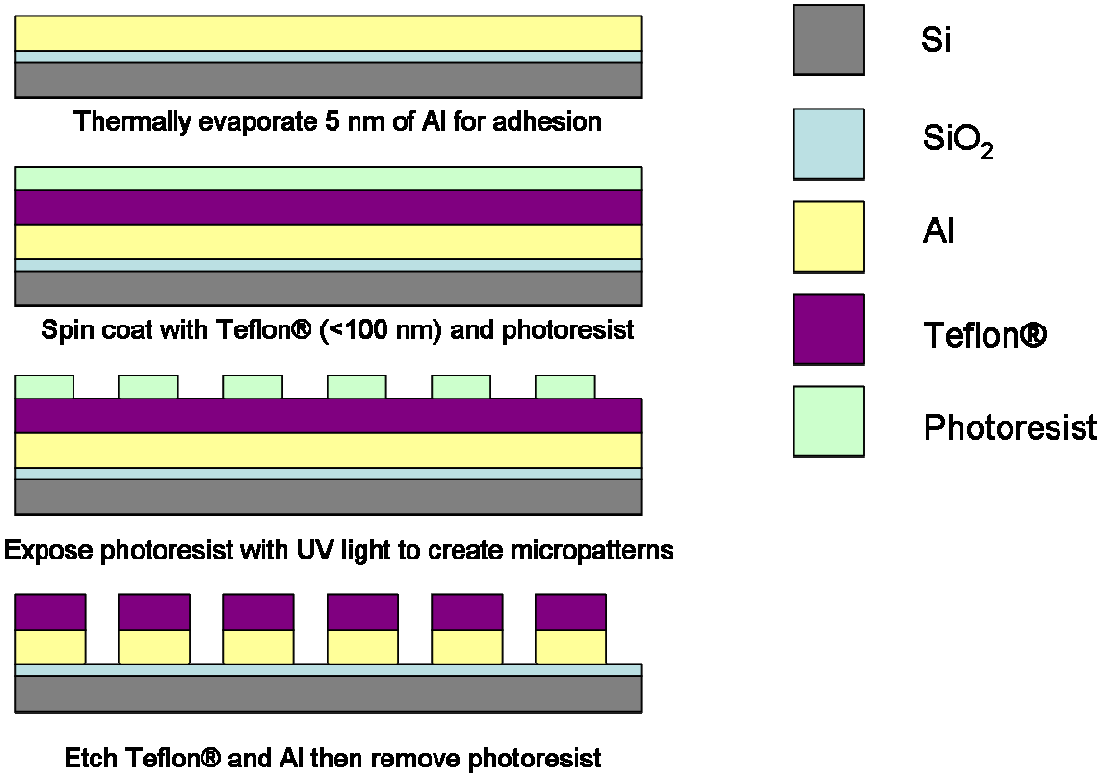

Figure 28: Manufacturing process for Teflon © patterning

Another manufacturing process using self-assembled monolayers of octadecyltrichlorosilane (OTS) on SiO_2 [77] was tested but abandoned because of delamination during the boiling experiments. On the bottom side of the wafer an Indium Tin Oxide (ITO) heater is sputtered, with thermally evaporated Copper electrodes. The heater is then passivated with a 100nm SiO_2 layer. A thin thermocouple (Omega CO2, K-type) is taped onto the center of the ITO heater using a polyimide adhesive pad. A 5mm thick PDMS layer is then used to seal the bottom side of the wafer. Optionally, a final step was added to increase the wettability, by rinsing for a few seconds the top side of the wafers with a diluted solution of buffered hydrofluoric acid (HF). The wettability was measured with a goniometer, with wetting angles of 110º for the Teflon, 10-25º for the

SiO_2 and 7º for the SiO_2 treated with HF. The maximum height of the patterns was 100 nm, while the roughness was below 5nm, as measured with a contact profilometer. No difference in pattern height was observed after the HF treatment.

4.3 Experimental set up

Heat transfer measurements are run using a pool boiling setup similar to the one in [73]. The wafer is placed in a polycarbonate chamber open to the atmosphere, filled with degassed, deionized water. The water is maintained at the saturation temperature of 100^oC by two immersed 100W cartridge heaters. A 750W power supply (Agilent N5750A) is used in constant voltage mode to apply a given heat flux to the 1 cm^2 ITO heater patterned on the back of the wafer. A data acquisition system (OMEGA DAQ-3000) is used to record the temperature measured on the back of the wafer, T_{meas}. The temperature at the wafer-water interface $T_w=T_{meas}-q''t/k$ is then determined using Fourier's law, with q'', t and k the respective heat flux, wafer thickness and Silicon thermal conductivity.

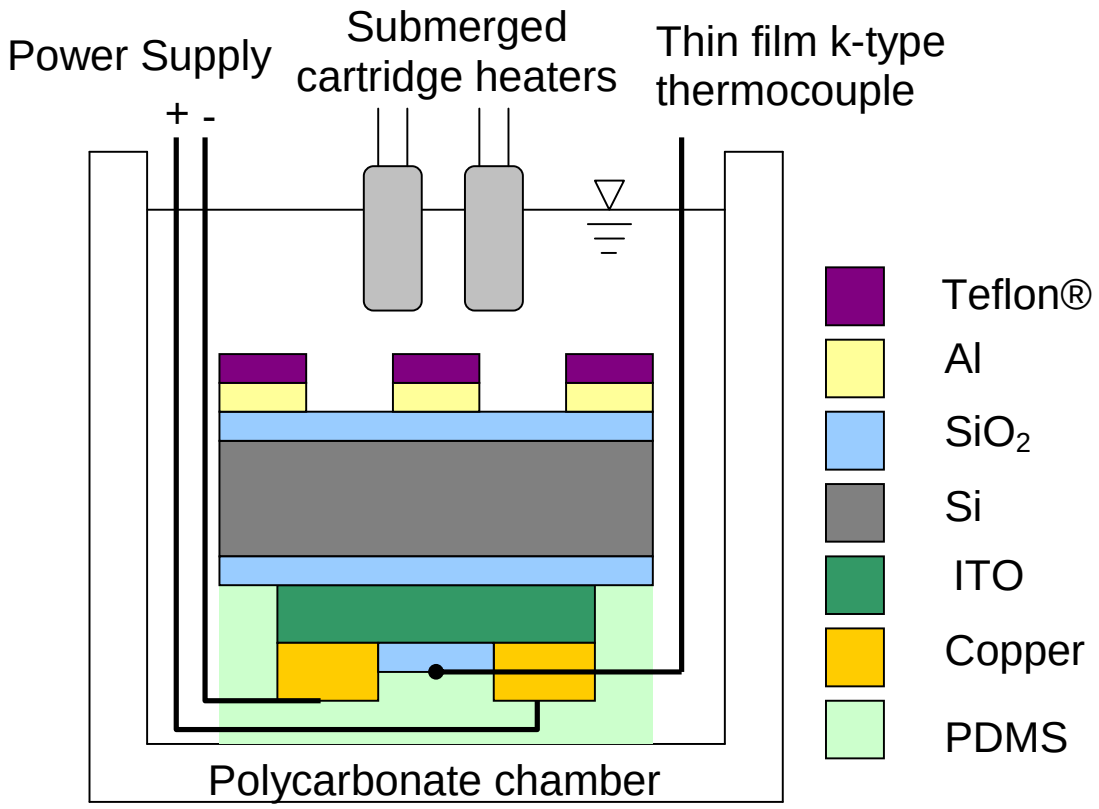

Figure 29: Experimental set up for pool boiling experiments.

For each data point presented in Figure 30, the temperature is obtained by averaging three hundred readings over about three minutes. The CHF is determined as the heat flux corresponding to the last observed stable temperature, beyond which a sudden dramatic increase in temperature is observed. The maximum combined uncertainty on the heat flux was estimated as ±1.5 W/cm^2, caused by the measurement of the heater area and the measurement of the electrical power. The maximum uncertainty on the superheat was estimated as ±1.5 K, due to the thermocouple uncertainty, temperature acquisition and heater/wafer thickness measurement uncertainties. For superheat values larger than 1 K the uncertainty on the heat transfer coefficient is typically 3 kW/m^{2}K.

4.4 **Results**

Measurements of boiling performance are shown in Figure 30, which compare the plain SiO_2 surfaces to surfaces featuring hydrophobic or hydrophilic networks. The pitch p was varied between 50 and 200 µm and an optional HF finishing is also mentioned. Figure 30a shows the typical heat flux q'' vs. superheat ΔT=Tw-Tsat curve. Values of CHF for a plain wafer treated with HF are about 115W/cm2 at ΔT=27K, consistent with the 100 W/cm2 at ΔT=33K obtained in [75] for a surface with slightly larger (18º degree) wetting angle, shown in Figure 31.

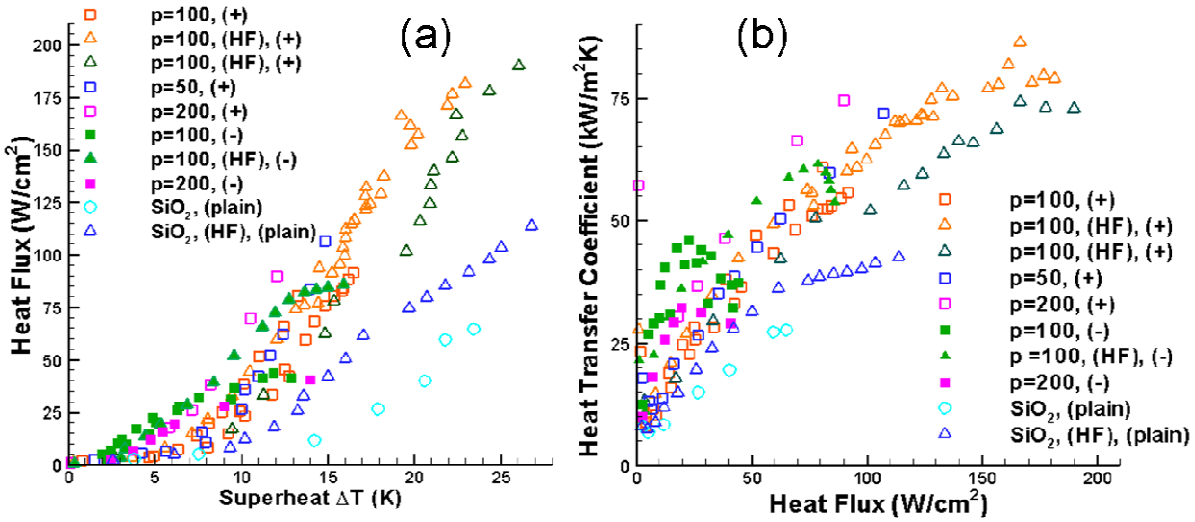

Figure 30: Boiling curves with measured heat flux as a function of the superheat (a) and heat transfer coefficient as a function of heat flux (b). Legend shows pitch p in µm and the presence of HF coating. Hydrophobic and Hydrophilic networks (see 1st figure) are designated by respectively (+) and (-).

All patterned surfaces exhibit a steeper boiling curve that the plane wafers, with critical heat fluxes ranging from 90 to 190 W/cm^2, up to 165% of the values of the plain wafer. The highest critical heat flux was reached for a pitch of 100 µm. Patterned surfaces

treated with HF exhibit a much higher heat flux than untreated patterned surfaces. In the three tested instances, hydrophobic networks exhibit a significantly lower CHF than the hydrophilic networks, sometimes even lower than plain SiO_2 surfaces. Figure 30b shows the heat transfer coefficient as a function of the heat flux. For heat fluxes lower than 50 W/cm^2, three groups of surfaces can be distinguished by their HTC. Plane surfaces exhibit the lowest HTC, hydrophilic networks show intermediate HTC values, and hydrophobic network show the maximum HTC values. For heat flux higher than 50 W/cm^2, the HTC of the hydrophilic networks increases to values up to $85kW/m^2$, which is twice the max HTC of the plain SiO_2 surfaces. As a summary, patterning of mixed hydrophilic and hydrophobic areas can improve the CHF and HTC of a plain hydrophilic surface by respectively 65 and 100%. While surfaces with hydrophilic networks enhance both the CHF and HTC, surfaces with hydrophobic networks seem to only enhance the HTC and might even reduce the CHF.

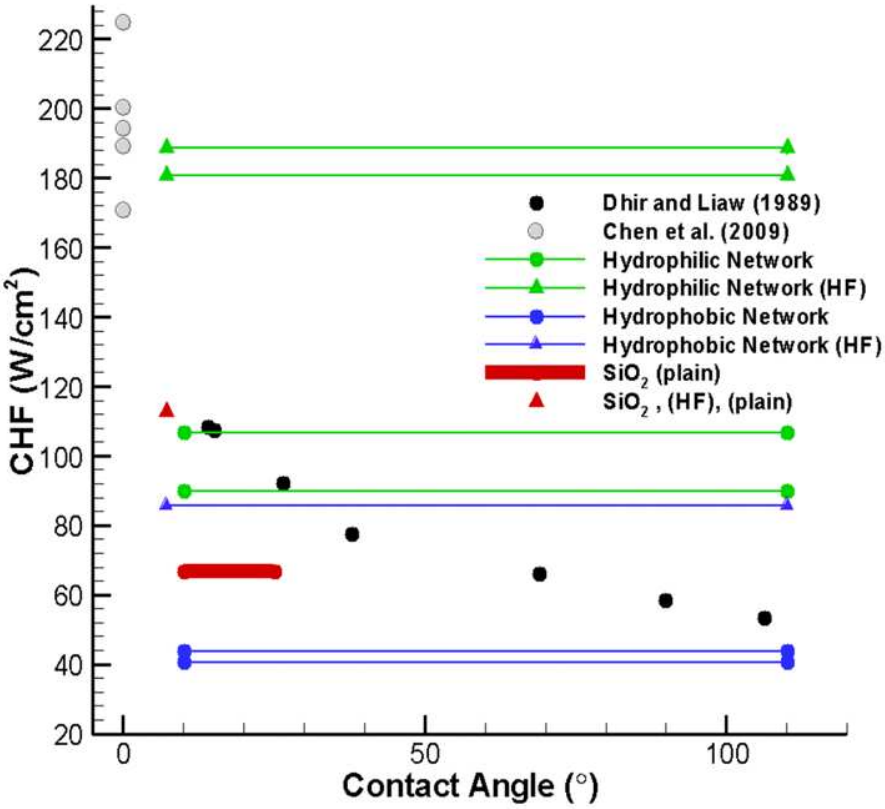

Figure 31: Critical Heat Flux as a function of wetting angle. Our results are in color, with horizontal lines for cases where the surfaces had mixed wetting properties. Black and grey dots are comparison data on respectively surfaces with controlled wetting properties and a superhydrophilic carpet of nanowires.

As shown by the comparison in Figure 31, the maximum values obtained in this work are comparable to the maximum HTC and CHF obtained on surfaces covered with a carpet of nanowires [72, 73], but slightly lower than sintered wicking surfaces such as in [70]. The surfaces studied in this work however are planar while the surface in [70, 72, 73] can be considered as extended surfaces and promote wicking transport. To emphasize the concept that that these enhanced surfaces have more than a unique value for the wetting angle, they are represented by horizontal lines rather than single points in Figure 31.

4.5 Discussion

Explaining the observed trends is complex because pool boiling is a transient, multiphase phenomenon, visualization is difficult especially for the violent boiling near CHF, and the geometry and wettability of these enhanced surfaces is complex. The following however can be said from the wide theoretical and experimental body of literature summarized in [66, 78, 79]. First, the enhancement of HTC on patterned surfaces can be explained by the increased availability of nucleation sites. Indeed, the nucleate boiling theory of Mikic and Rosenhow [80], states that $HTC = {q''}/{\Delta T} = K\sqrt{\pi\left(k_L \sigma C_p\right)} f D_b^2 Na$, where K is a constant independent of the wetting angle and fluid properties ($k_L\sigma C_p$), D_b is the bubble diameter, f is the bubble release frequency and n_a is the density of nucleation sites. By patterning nucleation sites, we increase the number of nucleation sites, to which HTC is directly proportional. Interestingly, experiments in Figure 27c repeatedly show that bubbles start nucleating on the edge of the patterns, with diameters D_b much smaller than the pattern diameter. Mikic and Rosenhow's theory might also explain why the HTC of hydrophobic networks is higher than the HTC of hydrophilic networks, since hydrophobic networks offer a larger hydrophobic area, therefore more nucleation sites. Second, the regular patterns might also constrain the distance between the nucleation sites, which can moderate instabilities and enhance the critical heat flux. Indeed, as stated by Zuber [66, 81], the dryout responsible for critical heat flux is caused by Helmoltz instabilities that merge individual bubble columns. On a plain surface the typical pitch p between the bubble columns is determined by the Taylor instability

$\lambda = 2\pi\sqrt{3\sigma / g(\rho_l - \rho_v)} = 2.7\text{mm}$ [66]. According to the same theory, the critical vapor velocity that triggers Helmoltz instabilities is inversely proportional to $\lambda^{-0.5}$. This analysis concludes to a maximum "practical" CHF value around 110 W/cm^2. Let's assume now that the regular patterns investigated in this study have the ability to constrain the wavelength of the instabilities to the pattern pitch λ_p. In that case, λ_p between 200 and 50 µm would multiply the attainable CHF by $(\lambda/\lambda_p)^{0.5}$, a factor between 11 and 23. For hydrophilic networks, the improvement measured experimentally is "only" 1.65, which indicates that other limiting factor might come into play. For instance the kinetic analysis by Schrage [82] determines that for water at atmospheric pressure an absolute theoretical upper bound for the CHF is 16.5 kW/cm^2. Third, the observed influence of HF in increasing CHF (but not HTC) can be explained by its increase of the wettability of the surface [74]. Fourth, the fact that hydrophilic networks show a large CHF enhancement, while hydrophobic networks do not show this CHF enhancement can be explained by the droplet boiling experiments in Figure 32, recorded with a high-speed camera. In both experiments, a 3 µL water droplet is gently deposited on a patterned surface heated to an initial temperature of 132ºC.

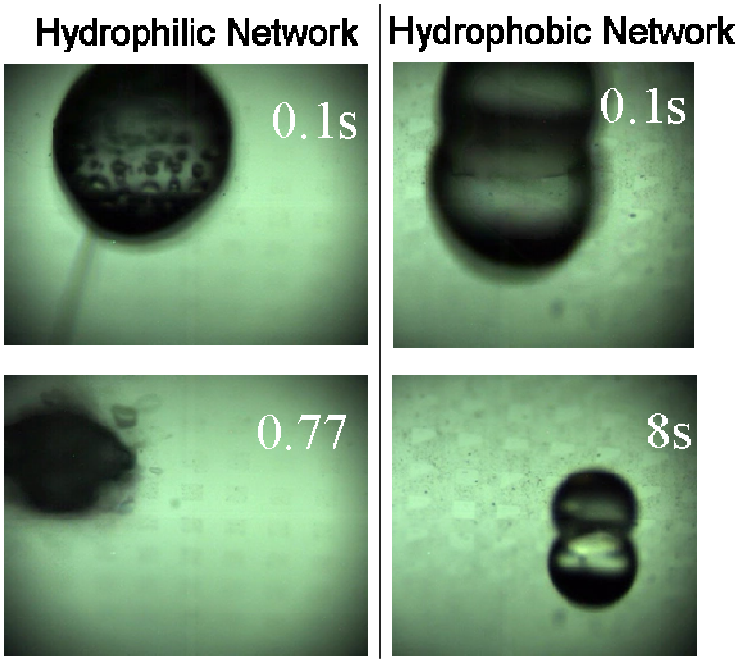

Figure 32: The evaporation of a 3 microliter water drop on two patterned surfaces heated at 132C, the left surface exhibiting a hydrophilic network and the right surface, a hydrophobic networks. For these experiments the patterns are square, with a pitch of 250 µm.

At 0.1s on the hydrophilic network (left), several individual bubbles have nucleated. A very dynamic boiling process occurs then, visible from the strong and fast perturbations on the drop free surface (t=0.77s). Despite the strong boiling, the drop does not move significantly, being hold to the substrate by the hydrophilic network. On the right, a similar drop is deposited on a hydrophobic network, and shows a completely different behavior: at t=0.1s, the drop does not seem to wet the substrate, as evidenced by the circular shadow under the drop. No individual bubbles are visible, and the drop moves towards the bottom right of the field of view during the evaporation. The total evaporation times of 11 seconds is one order of magnitude larger than the evaporation time on the hydrophilic network. The sliding, absence of individual bubbles, and larger evaporation time suggest the presence of an insulating vapor film between the bubble and

the substrate, analog to the Leidenfrost phenomenon. While the transient experiments in Figure 32 are not equivalent to the steady state pool boiling experiments, they suggest that hydrophobic networks help nucleation while preventing early the formation of a vapor film, while hydrophobic networks, where vapor bubbles can easily merge, favor early occurrence of CHF. Indeed the hydrophobic networks, unless treated with HF, exhibit a lower CHF than the bare SiO_2, probably because it promotes the formation of a vapor film. As a final observation, we note that the size of the patterns is compatible with the size of the active nucleation sites predicted by Hsu's theory [83]. It states that for a fluid at saturation temperature, the range of radii of active nucleation sites is $\{r_{\max}, r_{\min}\} = \frac{\delta}{2C_1}\left[1 \pm \sqrt{1 - \frac{4AC_3}{\delta\theta_w}}\right]$. In this equation, δ is the boundary layer thickness, C_1 = $(1+\cos\varphi)/\sin\varphi$, $C_3 = (1+\cos\varphi)$, φ is the wetting angle, $A = 2\sigma T_{sat}/\rho_v h_{Lv}$, and $\theta_w = T_w - T_{sat}$. For the constant heat flux case, assuming free convection and a linear temperature profile in the thermal boundary layer, with a wetting angle φ=110º corresponding to the Teflon surface, we obtain a boundary layer thickness of about 400 µm, corresponding to a range of active nucleation sites of 1 to 40 µm at a wall superheat ΔT=5ºC and 0.3-100µm at ΔT=20ºC. This size is compatible with the size of the hydrophobic patterns, which range from about 25 to 100 micrometer and exhibit offer smaller nucleation sites, as shown in Figure 27c.

In summary, it has been demonstrated that surfaces with networks combining hydrophilic and hydrophobic regions significantly enhance the critical heat flux and heat transfer coefficient during pool boiling. The best enhancement arises with hydrophilic networks

featuring hydrophobic islands, which efficiently prevent the formation of an insulating vapor layer.

5 ANALYTICAL MODEL TO PREDICT THE HEAT TRANSFER COEFFIECIENT OF A SURFACE OF HETEROGENEOUS WETTABILITY

5.1 Introduction

In chapter 4 surfaces with heterogeneous wettability were studied and they were found to enhance pool boiling heat transfer up to 100% compared to plain hydrophilic surface. The previous work also showed that the type of network connectivity influences the performance. In this chapter an existing analytical model was modified to explain the heat transfer enhancement on a hydrophilic network surface. This model will also serve as a framework to explore the large parameter space including the size and pitch of the patterns as well as the influence on the contact angles of both regions.

5.2 Liquid vapor exchange model

The liquid vapor exchange model proposed by Forster and Greif [84] postulates that bubbles act as micropumps and draw cold fluid in contact to the surface as they depart from the surface. In their model they find that the major heat transfer mechanism is transient conduction through the liquid film. To explain the observed enhancement of HTC we modified this analytical model, equation 1, for a heterogeneous wettability surface. The values for the bubble departure diameter d_d, frequency of bubble departure $\tilde{f}$ and the number of active nucleation sites n_a' can be found experimentally with high speed visualization; they can also be estimated using the following method.

$$\mathrm{HTC} = 2(\pi k_l \rho_l c_{pl})^{1/2} d_d^2 \tilde{f}^{1/2} n_a' \tag{25}$$

5.3 Calculating the bubble departure diameter

The departure diameter can be calculated by balancing surface tension and buoyancy forces. The departure diameter of a bubble from a homogeneous surface is plotted as a function of the contact angle in Figure 33a. Within the graph are diagrams that show the shape of the bubble as it grows and departs from a wetting (left) and a non-wetting (right) surface. For a heterogeneous surface we assume the bubble will become pinned to the non-wetting spot and the internal angle of the bubble will increase as it grows as shown in Figure 33b. Therefore the departure diameter is only a function of the non-wetting spot size. In our model, for simplicity, we assumed a circular spot.

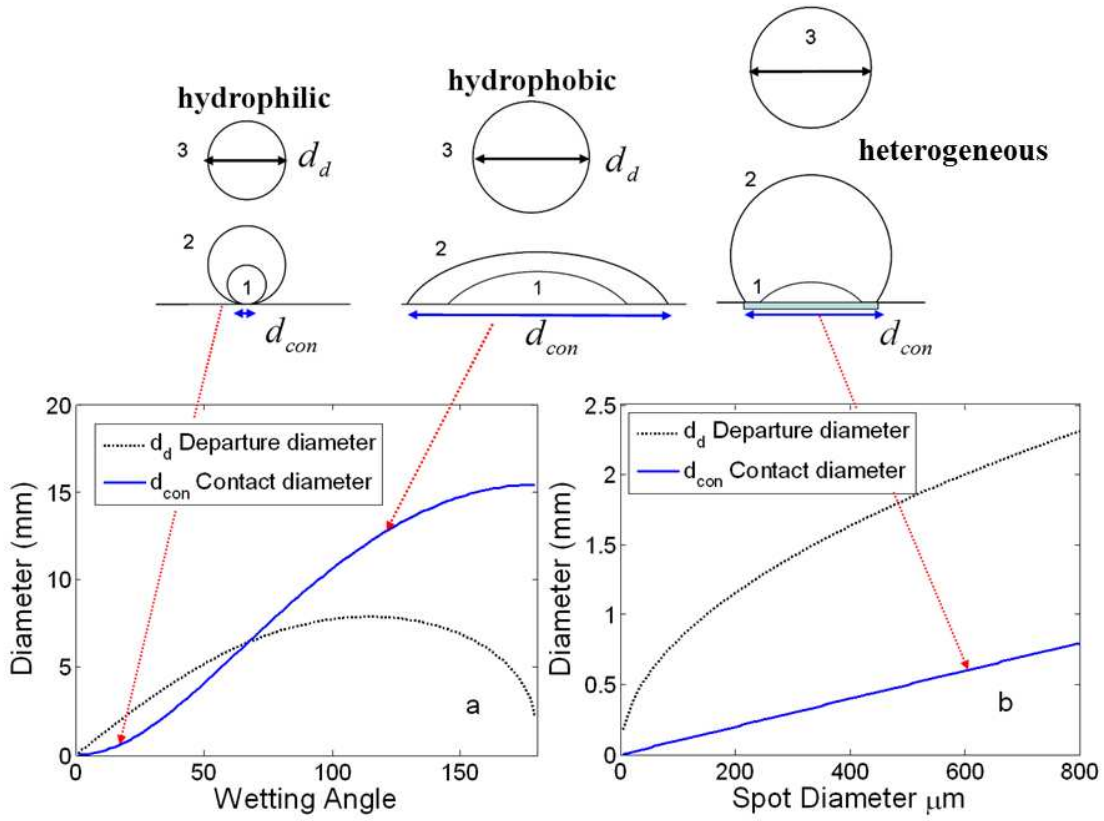

Figure 33: The departure diameter compared to the contact diameter of a bubble as (a) a function of wetting angle of a homogeneous surfaces and (b) as a function of the spot size for a heterogeneous surfaces. The cartoons above illustrate the contact and departure shape.

5.3.1 Frequency of bubble departure

The departure frequency is inversely proportional to the departure diameter [85]. Equation 26 is used to estimate the frequency of bubble departure [86]. The form of equation 26 is derived from the critical velocity required to obtain Kelvin-Helmholtz instabilities and the coefficient D is determined empirically.

$$\tilde{f}d_d = D\left[\frac{\sigma g(\rho_l - \rho_g)}{\rho_l^2}\right]^{1/4} \tag{26}$$

5.4 Determining the number of active nucleation sites

The active nucleation site density is difficult to estimate because it is dependent on the properties of the surface [87]. The theory of Hsu [88] can be used to find the range of active nucleation sites size as a function of superheat but a distribution that gives the number and size of the cavities on the surface is required to determine how many sites actually nucleate. Another option is to determine the number of active nucleation site experimentally. At the onset of boiling the number of active nucleation sites is small and can easily be counted from high speed movies. Several points at the onset at nucleation can be used to generate a curves for both the wetting and the non-wetting surface, since the number of active nucleation sites is proportional to the surface superheat $n_a^{'} \propto \Delta T^m$ [89]. However, the number of nucleation sites can not increase indefinitely; the surface will eventually become saturated by the bubbles. We impose two constraints for the maximum number a nucleation sites $n_{a,\max}^{'}$. First, for a heterogeneous surface $n_{a,\max}^{'}$ for the non-wetting spots cannot exceed the number of patterned spots. In other words there can only be one active nucleation site per spot. Second, for both homogeneous and heterogeneous surfaces we assume each bubble has a sphere of influence or an area around the bubble where is draws liquid from for bubble growth [90]. Therefore the maximum number of active nucleation sites is equal to the sphere of influence divided by the total heated area $n_{a,\max}^{'} = D\pi(d_d/2)^2 \Big/ A$.

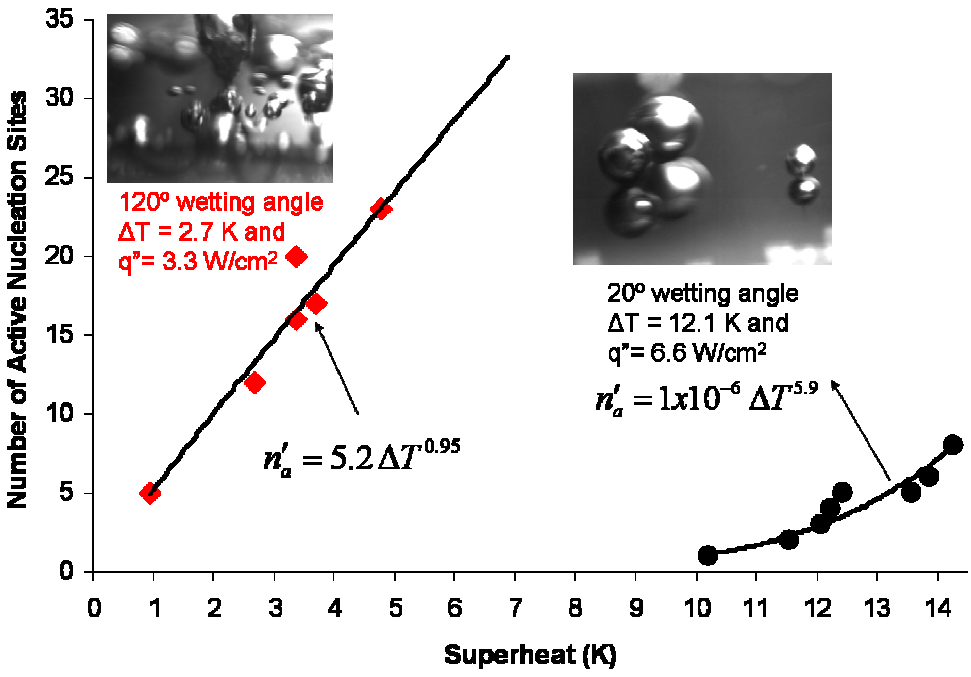

Figure 34: Number of active nucleation sites measured from high speed visualization for a hydrophobic surface with a wetting angle of 120° and for a hydrophilic surface with a wetting angle of 20°. From these measurements we can fit a curve for the number of active nucleation sites as a function of temperature.

5.5 Modified analytical model

We have determined all the variables (d_d, $\tilde{f}$ and $n_a^{'}$) to determine HTC (ΔT). For a heterogeneous surface, HTC is expressed by equation 3, where the HTC for the wetting surface is superimposed with a modified HTC for the non-wetting surface that includes the departure diameter from a non-wetting spot, as calculated in figure 3.

$$\mathrm{HTC} = 2(\pi k_l \rho_l c_{pl})^{1/2}\left[(\tilde{f}^{1/2} d_d^2 n_a^{'})_{wetting} + (\tilde{f}_{spot}^{\ 1/2} d_{d,spot}^2 n_a^{'})_{non-wetting}\right] \quad (27)$$

5.5.1 Comparison to experimental results

Figure 35 (left) shows that the model can predict HTC as a function of temperature for homogeneous and heterogeneous surfaces. The theoretical values for HTC of a SiO_2, Teflon and heterogeneous surface as predicted by the modified analytical model are compared to experimental values. The heterogeneous surface has 50 µm spots and a 100 µm pitch between patterns. On the right we can see the effect of varying the contact angle of the wetting surface. By decreasing the contact angle of the wetting surface the surface can reach higher HTC. At low superheat nucleation only occurs on the non-wetting spots and the HTC is independent of the wetting surface. At higher superheats when the wetting surface begins nucleating, lower contact angles produce smaller bubbles. The maximum HTC is higher because more sites can nucleate before the surface saturates with bubbles.

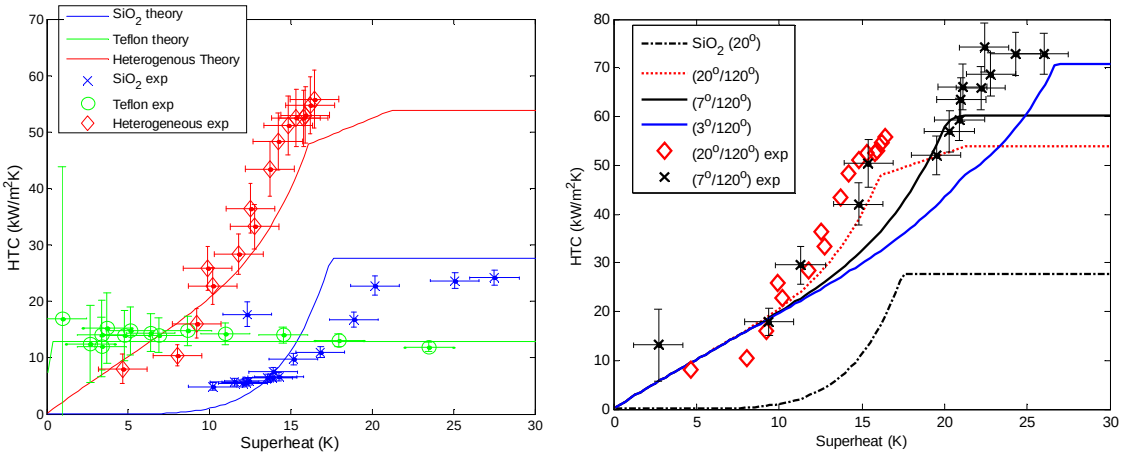

Figure 35: Comparison of the modified liquid-vapor exchange model to experiments on a plain SiO_2 and Teflon surfaces and a heterogeneous surface with 50 µm spots and a 100 µm pitch (left). Effect of varying the contact angle of the hydrophilic surfaces on HTC as a function of temperature (right). Both surfaces tested had 50 µm spots and a 100 µm pitch.

To further validate our model we looked at the effect of varying spot size (Figure 36). The spot size tested was 5, 50 and 400 µm. The samples were smooth surfaces with wetting angles of 20º for the silicon surface and 120º for the Teflon. For the 5 and 50 µm surfaces there is good agreement between the experiments and theory. For the 400 µm spot the agreement is not as good, but model accurately predict the trend that larger spots will produce higher HTC especially at low superheat.

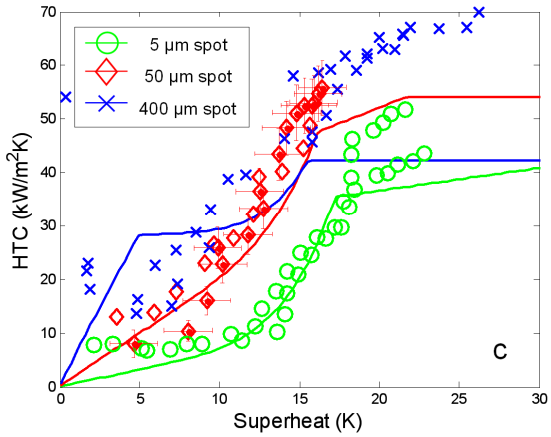

Figure 36: Comparison of analytical model to experimental results for spot sizes of 5, 50 and 400 µm. In all experiment the ratio of diameter to pitch was held constant d/p = 0.5.

5.6 Discussion

Our model explains why heterogeneous wettability surfaces can reach higher values of HTC. The non-wetting spots provide early onset of boiling and available nucleation sites but controls the bubbles departure size preventing the surface from being saturated with bubbles. This model also provides a theoretical frame work to design and optimize heterogeneous surfaces for pool boiling applications. In this model HTC is a function of temperature, spot size, pitch and contact angle of the wetting surface. It is also dependent on the available nucleation sites for both the wetting and non-wetting surface and the fluid. Since many pool boiling application require a specific heat flux or wall temperature, the optimal geometry is also a function of the operating conditions. Another piece of the puzzle is to develop a model to predict and optimize CHF for these heterogeneous wettability surfaces. Further investigation into the large parameter space of heterogeneous wettability surfaces is needed to develop them for widespread use.

6 SUMMARY AND FUTURE WORK

In this thesis several application for multiphase microfluidics are demonstrated and tested:

In Chapter 2 microfluidic methods were used to manufacture monodispersed microparticles of a novel hydrogel formulation. The microfluidic chip was designed based on previous work in flow focusing of viscous fluids [91] and fabricated using standard micromilling methods. The microfluidic method generated monodispersed particles with a coefficient of variance less than 7%. The achievement of this work is that the microparticles generated are both biodegradable and mechanically strong. This work is also the first demonstration of flow focusing with both viscous and reactive fluids.

In Chapter 3 a microchannel heat sink was modified to produce segmented flow of water and air. With the addition of segmented flow the heat transfer coefficient can be improved by 140% compared to single-phase flow of the same liquid flow rate and a 50% improvement was documented at the same pressure drop. Segmented flow has been previously used to enhance mass transfer in microchannels [7]. This work was the first time this flow pattern was made in multiple channels from a single fluid and air inlet. This work was also the first time segmented flow was used to enhance heat transfer.

In Chapter 4 heterogeneous wettability surfaces were manufactured and their pool boiling performance was tested. These surfaces can increase the heat transfer coefficient by

100% and the critical heat flux by 65% compared to a very hydrophilic surface. Heterogeneous wettability surfaces were previously studied in the 1960's [92, 93] but this was the first demonstration that they can simultaneously increase the heat transfer coefficient and the critical heat flux. New manufacturing methods allow for more precise control of the pattern thickness, shape and size, which ultimately provides better control of the heat transfer performance.

In Chapter 5 an analytical model to predict the heat transfer coefficient of surfaces with heterogeneous wettability was developed. The model proposed was in good agreement with experiments for heat transfer coefficients below 40 kW/m^2K. This model also provides insight into the physics of the heat transfer enhancement on heterogeneous wettability surfaces. Simple experiments to determine the number of active nucleation sites were performed at they showed that Teflon surface lower the onset of nucleate boiling and increases the number of active nucleation sites. By patterning the Teflon the size of departing bubbles and the contact area of bubbles can be controlled.

6.1 Future work

While heterogeneous wettability surfaces where first studied in the 1960's [92, 93], this work is the first demonstration of their effectiveness to increase both the heat transfer coefficient and the critical heat flux. The model presented in this work is the beginning of a theoretical frame work to design heterogeneous wettability surfaces. The following sections outline other areas of study for these surfaces to implement them for wide spread use.

6.1.1 Analytical model of the critical heat flux of a surface of heterogeneous wettability

This work demonstrates that existing analytical models for predicting the heat transfer coefficient can be modified for surfaces with heterogeneous wettability. This is only half of the performance of a boiling surface, it is necessary in many design application to be able to predict the critical heat flux. It is not obvious from our experiments what factors influence the critical heat flux. More experiments need to be preformed varying the spot size and pitch of the patterns as well varying the wettability of the surfaces to establish trends. Once these trends have been established the hydrodynamic model used to predict critical heat flux [67] can be reevaluated to determine if it can be modified for a heterogeneous surfaces.

6.1.2 Multiscale surface features for enhanced surfaces of heterogeneous wettability

As mentioned in the introduction multiscale surface have recently attracted attention for their heat and mass transport capabilities [10-12]. Engineering combined nano and microscale surface would be the next step to enhance heat transfer enhancement. Preliminary studies on multiscale surfaces have been presented by the author at conference proceedings [94].

6.1.3 Numerical modeling of pool boiling

Numerical modeling of boiling is complex due to its stochastic nature. On surfaces with regularly patterned nucleation sites the stochastic nature of boiling may be eliminated by

assuming the location of the nucleation sites. Numerical modeling will help gain insight into the fluid dynamics of the bubble departure, which can be used to further develop the analytical theories for the heat transfer coefficient and the critical heat flux.

6.1.4 Studies on the robustness of surfaces of heterogeneous wettability

In boiling the robustness of surfaces is extremely important. In boiling surfaces are exposed to high temperature gradient and shear stress. The longevity of a surface is also important in applications such as nuclear engineering since the boiling surfaces may need to last for 30 years. In this work the heterogeneous wettability surfaces appeared relatively robust but characteristics such longevity, maximum operating temperature, scratch resistance and fouling susceptibility were not study. However the heterogeneous wettability surfaces did last through several days of boiling experiments and several samples were undamaged by the onset of the critical heat flux. Also no damage occurred when a contact profilometer, which applied forces up to 100 mN, was used to measure the height of the patterns. A more detailed study of the physical performance of these surfaces is needed. Also, other lower cost materials and alternative manufacturing methods should be explored.

References

[1] Nguyen, N.-T. and S.T. Wereley, *Fundamentals and Applications of Microfluidics*, Artech House, 2002.

[2] Bruus, H., *Theoretical Microfluidics*. Oxford Master Series in Physics, Oxford University Press, 2008.

[3] Gunther, A. and K.F. Jensen, "Multiphase microfluidics: from flow characteristics to chemical and material synthesis", *Lab on a chip*, vol.6, pp. 1487-1503, 2006.

[4] Tuckerman, D.B. and R.F.W. Pease, "High-Performance Heat Sinking for VLSI.", *IEEE Electron Device Letters*, vol.EDL-2, pp. 126 -129., 1981.

[5] Cubaud, T., U. Ulmanella, and C.M. Ho, "Two-phase flow in microchannels with surface modifications", *Fluid Dynamics Research*, vol.38, pp. 772-786, 2006.

[6] Kreutzer, M.T., F. Kapteijn, J.A. Moulijn, and J.J. Heiszwolf, "Multiphase Monolith Reactors: Chemical reaction engineering of segmented flow in microchannels", *Chemical Engineering Science*, vol.5895-5916, 2005.

[7] Gunther, A., S.A. Khan, M. Thalmann, F. Trachsel, and K.F. Jensen, "Transport and reaction in microscale segmented gas liquid flow", *Lab on a chip*, vol.4, pp. 278-286, 2004.

[8] Amini, H. and D. DiCarlo. "Enhancement of Micro-Mixing Utilizing Inertial Flows Around Microspheres in Channel Flows". in *Proceedings of the 16th US National Congress of Theoretical and Applied Mechanics*, State College, PA, 2010.

[9] Christopher, G.F. and S.L. Anna, "Microfluidic methods for generating continuous droplet streams", *Journal of Physics D: Applied Physics*, vol.40, pp. R319-R336, 2007.

[10] Bocquet, L. and E. Lauga, "A smooth future?", *Nature Materials*, vol.10, pp. 334-337.

[11] Bhushan, B. and Y.C. Jung, "Wetting, adhesion and friction of superhydrophobic and hydrophilic leaves and fabricated micro/nanopatterned surfaces", *Journal of Physics Condensed Matter*, vol.20, pp., 2008.

[12] Sun, G., T. Gao, X. Zhao, and H. Zhang, "Fabrication of micro/nano dual-scale structures by improved deep reactive ion etching", *Journal of Micromechanics and Microengineering*, vol.20, pp., 2010.

[13] Ahn, H.S., C. Lee, H. Kim, H. Jo, S. Kang, J. Kim, J. Shin, and M.H. Kim, "Pool boiling CHF enhancement by micro/nanoscale modification of zircaloy-4 surface", *Nuclear Engineering and Design*, vol.240, pp. 3350-3360.

[14] Barthlott, W. and C. Neinhuis, "Purity of the sacred lotus, or escape from contamination in biological surfaces", *Planta*, vol.202, pp. 1-8, 1997.

[15] Lee, C. and C.J. Kim, "Influence of surface hierarchy of superhydrophobic surfaces on liquid slip", *Langmuir*, vol.27, pp. 4243-4248.

[16] Xiao, R., K.H. Chu, and E.N. Wang. "Controlled liquid dynamics on three-dimensional nanostructured surfaces". in *Proceedings of the ASME Micro/Nanoscale Heat and Mass Transfer International Conference 2009, MNHMT2009*, p. 271-274.

[17] McDonald, J.C., D.C. Duffy, J.R. Anderson, D.T. Chiu, H. Wu, O.J.A. Schueller, and G.M. Whitesides, "Fabrication of microfluidic systems in poly(dimethylsiloxane)", *Electrophoresis*, vol.21, pp. 27-40, 2000.

[18] De Geest, B.G., J.P. Urbanski, T. Thorsen, J. Demeester, and S.C. De Smedt, "Synthesis of monodisperse biodegradable microgels in microfluidic devices", *Langmuir*, vol.21, pp. 10275-10279, 2005.

[19] Rondeau, E. and J.J. Cooper-White, "Biopolymer microparticle and nanoparticle formation within a microfluidic device", *Langmuir*, vol.24, pp. 6937-6945, 2008.

[20] Seo, M., Z. Nie, S. Xu, M. Mok, P.C. Lewis, R. Graham, and E. Kumacheva, "Continuous microfluidic reactors for polymer particles", *Langmuir*, vol.21, pp. 11614-11622, 2005.

[21] Yang, C.H., Y.S. Lin, K.S. Huang, Y.C. Huang, E.C. Wang, J.Y. Jhong, and C.Y. Kuo, "Microfluidic emulsification and sorting assisted preparation of monodisperse chitosan microparticles", *Lab on a Chip - Miniaturisation for Chemistry and Biology*, vol.9, pp. 145-150, 2009.

[22] Zhang, H., E. Tumarkin, R. Peerani, Z. Nie, R.M.A. Sullan, G.C. Walker, and E. Kumacheva, "Microfluidic production of biopolymer microcapsules with controlled morphology", *Journal of the American Chemical Society*, vol.128, pp. 12205-12210, 2006.

[23] Nie, Z., M. Seo, S. Xu, P.C. Lewis, M. Mok, E. Kumacheva, G.M. Whitesides, P. Garstecki, and H.A. Stone, "Emulsification in a microfluidic flow-focusing device: Effect of the viscosities of the liquids", *Microfluidics and Nanofluidics*, vol.5, pp. 585-594, 2008.

[24] Rosaguti, N., "laminar flow and heat transfer in a periodic serpentine channel with semi-circular cross section", *International Journal of Heat and Mass Transfer*, vol.49, pp. 2912-2923, 2006.

[25] Yobas, L., S. Martens, W.-L. Ong, and N. Ranganathan, "High-performance flow-focusing geometry for spontaneous generation of monodispersed droplets", *Lab on a Chip - Miniaturisation for Chemistry and Biology*, vol.6, pp. 1073-1079, 2006.

[26] Tan, S.-H., S.M. Sohel Murshed, N.-T. Nguyen, T.N. Wong, and L. Yobas, "Thermally controlled droplet formation in flow focusing geometry: Formation regimes and effect of nanoparticle suspension", *Journal of Physics D: Applied Physics*, vol.41, pp., 2008.

[27] Utada, A., A. Fernandez-Nieves, H.A. Stone, and D.A. Weitz, "Dripping to Jetting Transitions in Coflowing Liquid Streams", *Physical Review Letters*, vol.99, pp., 2007.

[28] Upadhye, H.R. and S.G. Kandlikar. "Optimization of microchannel geometry for direct chip cooling using single phase heat transfer". in *Proceedings of the Second International Conference on Microchannels and Minichannels (ICMM2004)*, 2004, p. 679-685.

[29] Shah, R.K. and A.L. London, *Laminar Flow Forced Convection in Ducts: A source book for compact heat exchanger analytical data*. Advances in Heat Transfer, ed. T.F. Irvine and J.P. Hartnett. Vol. Supplement 1, Academic Press, 1978.

[30] Krishnamurthy, S. and Y. Peles, "Flow boiling water in a circular staggered micro-pin heat sink", *International Journal of Heat and Mass Transfer*, vol.51, pp. 1349-1364, 2008.

[31] Wang, Y., "Experimental investigation of heat transfer performance for a novel microchannel heat sink", *Journal of Micromechanics and Microengineering*, vol.18, pp., 2008.

[32] Escher, W., B. Michel, and D. Poulikakos, "Efficiency of optimized bifurcating tree-like and parallel microchannel networks in the cooling of electronics", *International Journal of Heat and Mass Transfer*, vol.52, pp. 1421-1430, 2008.

[33] Qu, W. and I. Mudawar, "Flow boiling heat transfer in two-phase micro-channel heat sinks", *International Journal of Heat and Mass Transfer*, vol.46, pp. 2755-2771, 2003.

[34] Tiantian, Z. and J. Li. "Laminar flow characteristics in entry region in microchannels". in *2008 Proceedings of the ASME Micro/Nanoscale Heat Transfer International Conference, MNHT 2008*, 2008, p. 1257-1264.

[35] Lee, P.-S. and S.V. Garimella, "Thermally developing flow and heat transfer in rectangular microchannels of different aspect ratios", *International Journal of Heat and Mass Transfer*, vol.49, pp. 3060-3067, 2006.

[36] Lee, J. and I. Mudawar, "Assessment of the effectiveness of nanofluids for single-phase and two-phase heat transfer in micro-channels", *International Journal of Heat and Mass Transfer*, vol.50, pp. 452-463, 2007.

[37] Tsai, T.-H. and R. Chein, "Performance analysis of nanofluid-cooled microchannel heat sinks", *International Journal of Heat and Fluid Flow*, vol.28, pp. 1013-1026, 2007.

[38] Mudawar, I., "Assessment of High-Heat-Flux Thermal Management Schemes", *IEEE Transactions on Components and Packaging Schemes*, vol.24, pp., 2001.

[39] Steinke, M.E. and S.G. Kandlikar, "An Experimental Investigation of Flow Boiling Characteristics of Water in Parallel Microchannels", *Journal of Heat Transfer*, vol., 2004.

[40] Agostini, B., M. Fabbri, J. Park, L. Wojtan, and J. Thome, "State of the Art of High Heat Flux Cooling Technologies", *Heat Transfer Engineering*, vol.28, pp. 258-281, 2007.

[41] Kandlikar, S., "High Heat Flux Removal with Microchannels-A Roadmap of Challenges and Opportunities", *Heat Transfer Engineering*, vol.26, pp. 5-14, 2005.

[42] Qu, W. and I. Mudawar, "Measurement and prediction of pressure drop in two-phase micro-channel heat sinks", *International Journal of Heat and Mass Transfer*, vol.46, pp., 2003.

[43] Mudawar, I. and M.B. Bowers, "Ultra-high critical heat flux (CHF) for subcooled water flow boiling-I: CHF data and parametric effects for small diameter tubes", *International Journal of Heat and Mass Transfer*, vol.42, pp. 1405-1428, 1999.

[44] Kuo, C.-J., A. Kosar, Y. Peles, S. Virost, C. Mishra, and M. Jensen, "Bubble Dynamics During Boiling in Enhanced Surface Microchannels", *Journal of Micromechanics and Microenginnering*, vol.15, pp. 1514, 2006.

[45] Kuo, C.-J. and Y. Peles, "Pressure effects on flow boiling instabilities in parallel microchannels", *International Journal of Heat and Mass Transfer*, vol.52, pp. 271-280, 2009.

[46] Kosar, A., C.J. Kuo, and Y. Peles, "Suppression of boiling flow oscillations in parallel microchannels by inlet restrictors", *Journal of Heat Transfer*, vol.128, pp. 251-260, 2006.

[47] Weinmueller, C., N. Hotz, A. Mueller, and D. Poulikakos, "On two-phase flow patterns and transition criteria in aqueous methanol and CO2 mixtures in adiabatic, rectangular microchannels", *International Journal of Multiphase Flow*, vol.35, pp. 760-772, 2009.

[48] Cubaud, T. and C.-M. Ho, "Transport of bubbles in square microchannels", *Physics of Fluids*, vol.16, pp., 2004.

[49] Menech, M.D., P. Garstecki, F. Jousse, and H.A. Stone, "Transition from squeezing to dripping in a microfluidic T-shaped junction.", *Journal of Fluid Mechanics*, vol.595, pp. 141-161, 2008.

[50] Thorsen, T., R.W. Roberts, F.H. Arnold, and S.R. Quake, "Dynamic pattern formation in a vesicle-generating microfluidic device", *Physical Review Letters*, vol.86, pp. 4163-4166, 2001.

[51] Steijn, V. and M. Kreutzer, "Velocity Fluctuations of segmented flow in microchannels", *Chemical Engineering Journals*, vol.135S, pp. 159-165, 2008.

[52] Lakehal, D., G. Larrignon, and C. Narayanan, "Computational Heat Transfer and Two-phase Topology in miniature tubes", *Microfluid nanofluid*, vol.4, pp. 261-271, 2008.

[53] Chen, W.L., "Gas-Liquid two-phase flow in micro-channels", *International Journal of Multiphase flow*, vol.28, pp. 1253-1247, 2002.

[54] Thulasidas, T.C., M.A. Abraham, and R.L. Cerro, "Bubble-Train Flow In Capillaries of Circular and Square Cross Section", *Chemical Engineering Science*, vol.50, pp. 183-199, 1994.

[55] Gunther, A., M. Jhunjhunwala, M. Thalmann, M.A. Schmidt, and K.F. Jensen, "Micromixing of miscible liquids in segmented gas-liquid flow", *Langmuir*, vol.21, pp. 1547-1555, 2005.

[56] Xu, J., R. Vaillant, and D. Attinger, "Porous membrane for bubbles removal in microfluidic channels: physical mechanisms and design criteria", *Microfluid Nanofluid*, vol., in review.

[57] Muzychka, Y.S. and M.M. Yovanovich, "Laminar Forced Convection Heat Transfer in the Combined Entry Region of Non-Circular Ducts", *ASME Journal of Heat Transfer*, vol., 2004.

[58] Churchill, S.W., "FRICTION-FACTOR EQUATION SPANS ALL FLUID-FLOW REGIMES.", *Chemical Engineering (New York)*, vol.84, pp. 91-92, 1977.

[59] Hetsroni, G., A. Mosyak, E. Pogrebnyak, and Z. Segal, "Heat Transfer of gas-liquid mixture in micro-channel heat sink", *International Journal of Heat and Mass Transfer*, vol.52, pp. 3963-3971, 2009.

[60] Wong, H., C.J. Radke, and S. Morris, "The motion of long bubbles in polygonal capillaries, part 2 Drag, fluid pressure and fluid flow", *Journal of Fluid Mechanics*, vol.292, pp. 95-110, 1995.

[61] Hazel, A.L. and M. Heil, "The steady propagation of a semi-infinite bubble into a tube of elliptical or rectangular cross-section", *Journal of Fluid Mechanics*, vol.470, pp. 91-114, 2001.

[62] Ajaev, V. and G.M. Homsy, "Modeling Shapes and Dynamics of Confined Bubbles", *Annual Review of Fluid Mechanics*, vol.38, pp. 277-307, 2006.

[63] Miyamoto, M., Y. Katoh, J. Kurima, S. Kurihara, and K. Yamashita, "Free convection heat transfer from vertical and horizontal short plates", *International Journal of Heat and Mass Transfer*, vol.28, pp. 1733-1745, 1985.

[64] Incorpera, F.P., *Fundamentals of Heat and Mass Transfer*. 5 th ed, John Wiley and Sons, 2002.

[65] Figiola, R.S. and D.E. Beasley, *Theory and Design for Mechanical Measurements*. 4th ed, Wiley, 2006.

[66] Carey, V., *Liquid-Vapor Phase Change Phenomena*, Taylor and Francis, 1992.

[67] Zuber, N., *Hydrodynamic Aspects of Boiling Heat Transfer*. 1959, University of California: Los Angeles.

[68] Nam, Y. and Y.S. Jua, "Bubble nucleation on hydrophobic islands provides evidence to anomalously high contact angles of nanobubbles", *Applied Physics letters*, vol.93, pp. 3, 2008.

[69] Wang, C.H. and V.K. Dhir, "ON THE GAS ENTRAPMENT AND NUCLEATION SITE DENSITY DURING POOL BOILING OF SATURATED WATER", *Journal of Heat Transfer-Transactions of the Asme*, vol.115, pp. 670-679, 1993.

[70] Weibel, J.A., S.V. Garimella, and M.T. North, "Characterization of evaporation and boiling from sintered powder wicks fed by capillary action", *international Journal of Heat and Mass Transfer*, vol.53, pp. 4204-4215, 2010.

[71] Chien, L.H. and R.L. Webb, "Visualization of pool boiling on enhanced surfaces", *EXPERIMENTAL THERMAL AND FLUID SCIENCE*, vol.16, pp. 332-341, 1998.

[72] Li, C., Z. Wang, P.I. Wang, Y. Peles, N. Koratkar, and G.P. Peterson, "Nanostructured copper interfaces for enhanced boiling", *Small*, vol.4, pp. 1084-1088, 2008.

[73] Chen, R., M.-C. Lu, V. Srinivasan, Z. Wang, H.H. Cho, and A. Majumdar, "Nanowires for enhanced boiling heat transfer", *Nano Lett*, vol.9, pp. 548-53, 2009.

[74] Dhir, V.K. and S.P. Liaw, "Framework for a unified model for nucleate and transition pool boiling", *Journal of Heat Transfer*, vol.111, pp. 739-746, 1989.

[75] Wang, C.H. and V.K. Dhir, "EFFECT OF SURFACE WETTABILITY ON ACTIVE NUCLEATION SITE DENSITY DURING POOL BOILING OF WATER ON A VERTICAL SURFACE", *Journal of Heat Transfer-Transactions of the Asme*, vol.115, pp. 659-669, 1993.

[76] Jones, B.J., J.P. McHale, and S.V. Garimella, "The Influence of Surface Roughness on Nucleate Pool Boiling Heat Transfer", *Journal of Heat Transfer-Transactions of the Asme*, vol.131, pp., 2009.

[77] Zhang, P. and H.H. Qiu, "Investigation of the patterned surface modification on 3D vortex flow generation in a micropipe", *Journal of Micromechanics and Microengineering*, vol.18, pp. 8, 2008.

[78] Dhir, V.K., "Boiling heat transfer", *Annual Review of Fluid Mechanics*, vol.30, pp. 365-401, 1998.

[79] Pioro, I.L., W. Rohsenow, and S.S. Doerffer, "Nucleate pool-boiling heat transfer. I: review of parametric effects of boiling surface", *International Journal of Heat and Mass Transfer*, vol.47, pp. 5033-5044, 2004.

[80] Mikic, B.B. and W.M. Rohsenow, "A NEW CORRELATION OF POOL-BOILING DATA INCLUDING EFFECT OF HEATING SURFACE CHARACTERISTICS", *Journal of Heat Transfer*, vol.91, pp. 245-&, 1969.

[81] Zuber, N., *Hydrodynamic Aspects of Boiling Heat Transfer, AEC report AECU-4439*. 1959.

[82] Schrage, R.W., *A theoretical study of interphase mass transfer*, Columbia University Press, New York NY, 1953.

[83] Hsu, K.-Y., "On the size range of active nucleation cavities on a heating surface", *Asme Journal of Heat Transfer*, vol.84, pp. 207-216, 1962.

[84] Forster, H.K. and R. Greif, "Heat Transfer to a Boiling Liquid - mechanisms and correlations", *Journal of Heat Transfer*, vol.81, pp. 45, 1959.

[85] Carey, V.P., *Liquid-vapor-phase-change phenomena*, Taylor and Francis, 1992.

[86] Mikic, B.B. and W.M. Rohsenow, " A New Correlation of Pool-Boiling Data Including Effect of Heating Surface Characteristics", *Journal of Heat Transfer*, vol.91, pp. 245, 1969.

[87] Dhir, V.K., "Mechanistic prediction of nucleate boiling heat transfer-achievable or a hopeless task?", *Journal of Heat Transfer*, vol.128, pp. 1-12, 2006.

[88] Hsu, Y.Y., "On the Size Range of Active Nucleation Cavities on a Heating Surface", *Journal of Heat Transfer*, vol.207-216, 1962.

[89] Kandlikar, S.G., M. Shoji, and V.K. Dhir, eds. *Handbook of Phase Change: Boiling and Condensation*. 1999, Taylor and Francis.

[90] Han, C.-Y. and P. Griffith, "The Mechanism of Heat Transfer in Nucleate Pool Boiling - Part II", *International Journal of Heat and Mass Transfer*, vol.8, pp. 905-914, 1965.

[91] Anna, S.L., N. Bontoux, and H.A. Stone, "Formation of dispersions using "flow focusing" in microchannels", *Applied Physics Letters*, vol.82, pp. 364-366, 2003.

[92] Henley, J.J. and R.L. Hummel, "A third factor in boiling nucleation", *Industrial and Engineering Chemistry Fundamentals*, vol.6, pp. 603-606, 1967.

[93] Hummel, R.L.,"Means for Increasing the Heat Transfer Coefficient Between a Wall and Boiling Liquid",1965,patent number: 3,207,209

[94] Betz, A.R., J.R. Jenkins, C.J. Kim, and D. Attinger. "Significant boiling enhancement with surfaces combining superhydrophilic and superhydrophobic patterns". in *Proceedings of the IEEE International Conference on Micro Electro Mechanical Systems (MEMS)*, p. 1193-1196.